Proteomic analyses identify targets, pathways, and cellular consequences of oncogenic KRAS signaling

Authors: Nicole Kabella[1], Florian P. Bayer[1], Konstantinos Stamatiou[2], Miriam Abele[3], Amirhossein Sakhteman[1], Yun-Chien Chang[1], Vinona Wagner[4,5], Antje Gabriel[4,5], Johannes Krumm[8], Maria Reinecke[1,8], Melanie Holzner[8], Michael Aigner[1], Matthew The[1], Hannes Hahne[8], Florian Bassermann[4,5,6,7], Christina Ludwig[3], Paola Vagnarelli[2], Bernhard Kuster[1,6,7,*]

Affiliations:

[1]School of Life Sciences, Technical University of Munich, Freising, Germany

[2]College of Health, Medicine and Life Science, Brunel University London, London, UK

[3]Bavarian Center for Biomolecular Mass Spectrometry (BayBioMS), School of Life Sciences, Technical University of Munich, Freising, Germany

[4]Department of Medicine III, Klinikum Rechts der Isar, Technical University of Munich, Munich, Germany

[5]TranslaTUM, Center for Translational Cancer Research, Technical University of Munich, Munich, Germany

[6]German Cancer Consortium (DKTK), partner site Munich, a partnership between DKFZ and University Medical Center Technical University of Munich, Germany

[7]Bavarian Cancer Research Center (BZKF), Erlangen, Germany

[8]OmicScouts GmbH, Freising, Germany

*Corresponding author. Email: kuster@tum.de

Abstract

Mutations that activate the small GTPase KRAS are a frequent genetic alteration in cancer, and drug discovery efforts have led to inhibitors that block KRAS activity. We sought to better understand oncogenic KRAS signaling and the cytostatic effects of drugs that target this system. We performed proteomic analyses to investigate changes in protein abundance and posttranslational modifications in inhibitor-treated human KRAS-mutant pancreatic (KRAS G12C and G12D) and lung cancer (KRAS G12C) cells. The inhibitors used target these mutant forms of KRAS, the downstream effectors MEK and ERK, and the upstream regulators SHP2 and SOS1. Comparisons of phosphoproteomes between cell lines revealed a core KRAS signaling signature as well as cell line–specific signaling networks. In all cell lines, phosphoproteomes were dominated by different degrees of autonomous, oncogenic KRAS activity. Comparison of phosphoproteomes after short and long drug exposures revealed the temporal dynamics of KRAS-MEK-ERK axis inhibition that resulted in cell cycle exit. This transition to a quiescent state occurred in the absence of substantial proteome remodeling but included broad changes in protein phosphorylation and ubiquitylation. The collective data reveal new insights into oncogenic KRAS signaling, place many additional proteins into this functional context, and implicate cell cycle exit as a mechanism by which cells evade death upon KRAS signaling inhibition.

Introduction

Because drugs often have more than one target and the wiring of signaling pathways in cancer cells can be highly diverse, drug treatments sometimes lead to unexpected cellular effects (*1–4*). Proteomics approaches have greatly improved our understanding of the molecular and cellular mechanisms of action (MoA) of cancer drugs, and selective compounds are increasingly used as chemical probes to study the oncogenic signaling networks that these drugs perturb (*5–7*). Understanding the consequences of drug perturbation of the RAS-MEK-ERK axis as one of the most frequently activated pathways in cancer is particularly important. Proteomic analysis following the pharmacological targeting of key nodes within the mitogen-activated protein kinase (MAPK) pathway, such as the kinases ERK and MEK and the small GTPase KRAS, and across different cellular contexts, show dynamic responses (*8–10*). A notable example is a study of the ERK-regulated phosphoproteome in KRAS-mutated pancreatic cancer cells following drug perturbation. It suggests that >4,600 phosphorylation sites on >2,100 proteins are directly dependent on ERK activity, implying a broader role of ERK in cancer than hitherto appreciated (*11*).

Given the many functions of ERK for healthy physiology, it is currently unclear if target-related toxicity of ERK inhibition can be adequately managed. In fact, ERK inhibitors have not yet moved beyond phase 1 and 2 clinical evaluation, in contrast to the approval of four MEK and two KRAS inhibitors. The latter have received much attention because oncogenic mutations in *KRAS* that decouple KRAS activity from upstream signals are detectable in ~10-20% of all cancers (according to The Cancer Genome Atlas database, TCGA) with G12C being most prevalent in lung and G12D in pancreatic cancer (*12*). The approval of the two KRAS G12C drugs sotorasib and adagrasib, which covalently bind the mutated amino acid Cys^{12} and trap KRAS G12C in its inactive state, marked a milestone in KRAS drug discovery (*13–15*). Such mutant-specific drugs are attractive because they limit the risk of side effects resulting from target engagement in healthy tissues that also rely on the KRAS pathway for normal function. A number of further modalities are being investigated including inhibitors of KRAS G12D, pan-KRAS inhibitors, compounds directed against active GTP-bound KRAS, KRAS degraders, or drug combinations addressing upstream [the receptor tyrosine kinase EGFR, the phosphatase SHP2 (also called PTPN11), the guanine nucleotide exchange factor SOS1] or downstream (MEK, ERK) members of the KRAS signaling network that may offer treatment options for a broader range of patients (*16–19*).

The cellular MoAs of mutant-specific KRAS inhibitors (KRASi) have not yet been comprehensively characterized on a proteome-wide scale. We addressed this gap by measuring the concentration-response characteristics of target binding, pathway engagement, and cellular proteostasis of sotorasib, adagrasib, ARS-1620, MRTX1257 (KRAS G12C inhibitors; G12Ci) and MRTX1133 (KRAS G12D inhibitor; G12Di), complemented by inhibitors targeting upstream (SHP2, SOS1) and downstream (MEK, ERK) proteins in two KRAS-mutated pancreatic (KRAS G12C and G12D) cell lines and one lung cancer (KRAS G12C) cell line. Analysis of the resulting 715,239 concentration-response curves highlighted a common KRAS core signaling signature as well as differences between cell lines, placing hundreds of new proteins and their posttranslational modifications (PTMs) into the functional context of KRAS signaling. Our data demonstrated that oncogenic KRAS activity dominated the output of MEK and ERK activity and largely but incompletely decoupled KRAS from upstream receptor tyrosine kinase signaling, leading to exit of cells from the cell cycle and transitioning into a quiescent state. Furthermore, we found that dynamic protein phosphorylation and ubiquitylation,

rather than changes in protein abundance, were the main drivers of these processes, which included inhibition of kinases, transcription factors, and a likely ubiquitylation-mediated inactivation of E1 ubiquitin-activating and E2 ubiquitin-conjugating enzyme activities. We anticipate that the molecular resources provided alongside this manuscript and available in ProteomicsDB.org (*20*) will be of substantial utility for the scientific community for research on the KRAS signaling system and drugs to treat KRAS mutant cancer.

Results

Concentration-dependent, proteome-wide characterization of KRAS signaling inhibitors

The cellular MoAs of many KRAS inhibitors and other drugs acting on the RAS-MEK-ERK axis remain incompletely understood. To address this, we systematically measured the concentration-response characteristics of drug action characterized by potency (effective concentration to achieve 50% response; EC_{50}) and response (curve fold change) on a proteome-wide scale (Fig. 1). Including the EC_{50} dimension is powerful because it enables deducing both common as well as distinct responses in the same cellular system. We term this approach decryptE for proteins and decryptM for PTMs (*5*, *21*). Here, we applied both methods to characterize inhibitors targeting the RAS-MEK-ERK axis and extended the concentration-response idea to reactive cysteine profiling for drug-target deconvolution of cysteine-targeting covalent KRAS inhibitors (decryptC) (fig. S1,A and B) (*22*). Statistical analysis of all concentration-response data was performed by CurveCurator (*23*) followed by removal of outliers or manual inspection if required (fig. S2; see Materials and Methods for details). We initially focused on the FDA-approved KRAS G12C inhibitors sotorasib and adagrasib, their pre-clinical derivatives ARS-1620 and MRTX1257, and the KRAS G12D inhibitor MRTX1133. We then expanded the drug selection to compounds targeting proteins upstream and downstream of KRAS (for treatment-related information see data file S1). For cell line models, we chose the pancreatic cancer lines MiaPaCa-2 (KRAS G12C, homozygous) and ASPC1 (KRAS G12D, homozygous) as well as the lung cancer line NCI-H23 (KRAS G12C, heterozygous). These lines exhibited reduced viability in response to KRAS inhibition and represent cancer entities with high clinical prevalence of KRAS G12C or G12D substitutions (fig. S3; data file S2). Collectively, the different decrypt data types covered 25,038 cysteine-containing peptides (cys-peptides), 69,729 phosphopeptides, 13,093 ubiquitylated peptides (ubi-peptides) and 11,645 protein groups (Fig. 1; fig. S1B; data files S3–S6). Reproducibility of decryptM experiments was assessed by triplicate analysis of phosphoproteomes in response to sotorasib in MiaPaCa-2 cells showing that 80% of all EC_{50} values and curve fold changes were reproducible within a factor of two (fig. S4, A and B) (*5*). All data can be explored in ProteomicsDB (*20*) or through interactive html dashboards provided on Zenodo.org.

DecryptC profiling demonstrates high target selectivity of clinical KRAS G12C inhibitors

For in cellulo target deconvolution of the KRAS G12C inhibitors sotorasib and adagrasib, we applied competitive reactive cysteine profiling in two KRAS G12C and one KRAS G12D (as control) cell lines following 2 hours of drug treatment as previously described (*22*) but extending it here to full concentration-response measurements (fig. S1A; data file S1; data file S3). Between 12,500 and 18,600 cys-peptides were covered per cell line. Both G12C inhibitors potently modified Cys^{12} of KRAS in the two G12C cell lines. The potencies of the drug-target

interactions (EC_{50}) were determined to be 30 nM and 39 nM for sotorasib and 5nM and 14 nM for adagrasib in MiaPaCa-2 and NCI-H23 cells, respectively (Fig. 2,A and B). These potencies were in line with cell viability data (EC_{50} of 2-7 nM) collected after 72 hours of drug incubation, confirming that the inhibition of KRAS was responsible for the observed phenotypic effect (fig. S3; data file S2). Elongation factor EEF1A2 was identified as a new, but weak (1-3 µM), off-target of adagrasib (but not sotorasib) by covalently binding Cys^{31} in all cell lines (Fig. 2C). Molecular docking showed that the reactive group of adagrasib points to Cys^{31} and highlighted an additional interaction between EEF1A2 Tyr^{86} and the nitrogen of the methylpyrrolidine ring of adagrasib that does not exist in sotorasib (Fig. 2D). Very few additional cys-peptides showed reduced abundance in G12C cell lines which were not changed in the G12D line. Notable examples are two cys-peptides of the transcription factor ETV5 (Cys^{339}, Cys^{499}; Fig. 2A), which showed equipotent abundance reduction in MiaPaCa-2 cells in response to sotorasib and adagrasib, and their EC_{50} values were comparable to that of Cys^{12} from KRAS G12C (fig. S5A). However, these cases are unlikely to represent *bona-fide* off-targets but are more likely to result from changes in protein abundance due to transcriptional alterations elicited by KRAS inhibition. This interpretation is in line with total proteome analysis following 2h of drug treatment showing concentration-dependent protein reduction for several other short-lived transcription factors (MYC, JUN, FOSL1, EGR1) with similar potencies to the one observed for ETV5 (Cys^{339} and Cys^{499}; fig. S5B-D). Although we could not detect ETV5 in the deep-fractionated proteome of MiaPaCa-2 cells, published data demonstrate reduced mRNA and protein levels of ETV5 in response to U0126, a noncovalent inhibitor of MEK (*24*). Therefore, we conclude that adagrasib and sotorasib are highly selective binders of KRAS G12C in cells and qualify as chemical probes to study KRAS signaling.

DecryptM profiling demonstrates selective pathway engagement of KRAS inhibitors

To examine how inhibition of mutant KRAS affects downstream signaling, we subjected sotorasib, adagrasib, ARS-1620 and MRTX1257 (targeting KRAS G12C), and MRTX1133 (targeting KRAS G12D) to decryptM profiling of the phosphoproteome using the same cell lines and timing (2 hours) as above (fig. S1A; data file S1; data file S4). The timing was chosen to allow efficient target binding for covalent inhibitors while minimizing drug-induced changes in protein abundance (fig. S5B; fig. S6A), yet allowing sufficient time for full signaling pathway engagement (fig. S6B). In KRAS G12C cell lines, KRAS G12C–specific drugs changed the abundance of fewer than 600 phosphopeptides (of >20,000 recorded in each experiment; Fig. 3A). In contrast, MRTX1133 led to abundance changes of nearly 2,000 phosphopeptides in ASPC1 (KRAS G12D). Essentially no changes in the phosphoproteome were induced in sotorasib- or adagrasib-treated ASPC1 cells, demonstrating high selectivity of these KRAS G12C inhibitors for engaging KRAS-driven and phosphorylation-mediated cellular processes within the chosen drug concentration range. These experiments also demonstrated that the aforementioned weak off-target of adagrasib (EEF1A2 Cys^{31}; Fig. 2, C and D) was of no consequence to protein phosphorylation.

As expected, KRAS inhibition led to abrogation of MAPK1/3 activity, measured by the reduction of its activation loop phosphorylation status (Fig. 3B). No such effect was observed for KRAS G12C inhibitors in ASPC1 cells (KRAS G12D). The potency of MAPK1/3 inhibition closely mirrored the decryptC target binding and cell viability data, demonstrating that the drugs fully engaged the RAS-MEK-ERK axis in cells and were responsible for the observed inhibition of cell growth (Fig. 3C; fig. S3; data file S2). The concentration-dependent abundance changes

for each phosphopeptide in response to each drug and across cell lines (expressed as $pEC_{50} = -\log_{10}(EC_{50})$) revealed distinct potency profiles (Fig. 3D). Among the inhibitors, MRTX1257 showed the highest potency (apex at EC_{50} of 0.37 nM) and ARS-1620 was the least potent (apex at EC_{50} of 398 nM). In addition, the pEC_{50} distributions were mostly unimodal, and their apex EC_{50} values were close to the potency of reactive cysteine profiling and cell viability data (Fig. 3C-E). Therefore, the observed changes in the phosphoproteome can be attributed to KRAS inhibition.

Many phosphopeptides of described MAPK pathway members (according to KEGG: hsa04010; data file S7) showed abundance changes within a similar EC_{50} range (Fig. 3D, boxplots). Following a guilt-by-association logic, we concluded that many phosphopeptides with EC_{50} values close to known KRAS or MAPK pathway members may indeed themselves be functionally linked to the KRAS pathway. To define this pathway-associated group of phosphopeptides, the data was filtered to retain only phosphopeptides that were within ±1 pEC_{50} of the apex of each experiments pEC_{50} distribution(fig. S6, C and D).

We next asked to what extent phosphopeptides were affected by KRAS inhibitors in the same or different cell lines. Nearly 94% and 90% of all phosphopeptides showed consistent behavior in response to adagrasib and sotorasib in MiaPaCa-2 and NCI-H23 cells, respectively (Fig. 3F, fig. S7). Pairwise comparison of all drug responses in all cell lines using the mean absolute error (MAE) of the log2 curve fold change as a similarity metric, grouped the data by cell line, not by drug (Fig. 3G; fig. S7). This suggests that the different KRAS drugs act by essentially the same MoA in a given cell line but that the molecular composition and wiring of the KRAS pathway is substantially different between cell lines.

Identification of a common KRAS core signaling signature connecting multiple cellular processes

The very high target binding and pathway engagement specificity and selectivity of KRAS inhibitors observed above suggested that the 2,354 phosphopeptides showing short-term (2-hour) drug-induced abundance changes detected in the three cell lines (Fig. 4A) may be members of a wider oncogenic KRAS signaling network. Despite substantial response diversity between the three cell lines, a set of 241 phosphopeptides showed consistent abundance changes in all cell lines regardless of cancer entity, G12C or G12D mutant state, or hetero- or homozygosity of the KRAS locus (Fig. 4A; fig. S8A; data file S8). In the following, we refer to these as the KRAS core signaling signature. These 241 phosphopeptides comprise 252 phosphosites on 196 proteins (canonical sequences of protein coding genes, fig. S8B). We compared our data at the phosphosite level to three molecular resources: i) the ERK compendium (8), ii) a study by Klomp *et al*. focused on the ERK-dependent phosphoproteome (*11*), and iii) all regulatory phosphosites annotated in PhosphoSitePlus (phosphosite.org). The first two contain perturbation data using cell lines with mutations in *KRAS* or other oncogenes such as *BRAF* as well as cells stimulated with epidermal growth factor (EGF) to activate MAPK signaling. The latter resource is entirely biology-agnostic. Despite a large overlap of our data to these resources in terms of phosphoproteome coverage (71% overlap with the ERK compendium, 87% with the ERK-dependent phosphoproteome and 22% with PhosphoSitePlus; fig. S8C), the number of shared phosphosites with drug-induced abundance changes was relatively low (Fig. 4B). This discrepancy may be attributed to several factors. Other resources identified abundance changes on the basis of p-values from replicate experiments of high single-concentration drug treatments,

whereas we employed concentration-response statistics. Furthermore, these resources did not all use the same cell lines, and the drug treatment times were not identical. Still, 67% of the KRAS core signaling signature defined above was also contained in the ERK compendium and the ERK-regulated phosphoproteome published by Klomp *et al.*, underscoring its robustness (Fig. 4B).

Kinase motif enrichment analysis (*25*, *26*) (phosphosite.org) of the KRAS core signaling signature highlighted an over-representation of motifs that can be phosphorylated by ERK (MAPK1/3; SP/TP motif) and several members of the RSK, MNK and S6K families (basophilic motif) (Fig. 4C; data file S7). This is supported by the observation that several phosphosites known to regulate the activity of these kinases displayed reduced abundance upon treatment with KRAS-targeting drugs (according to phosphosite.org; Fig. 3B; fig. S9A)(*27*). The very same kinases also dominated when performing kinase motif enrichment analysis using all drug-affected phosphopeptides (fig. S9B; data file S7). About 51% (124/241) of the peptides in the KRAS signaling signature were phosphorylated at a SP/TP site, and several of these are annotated substrates of MAPK1 and MAPK3, including the transcription factor ERF (Thr^{562}; fig. S9C)(*28*).

Given the pronounced inhibition of MAPK1/3 activation loop phosphorylation by KRAS inhibitors, we hypothesized that many of the hitherto uncharacterized SP/TP motif–containing phosphorylation sites may be previously unidentified MAPK1/3 substrates. To test this, we performed in vitro kinase assays using recombinant MAPK1 and synthetic peptide substrates and monitored phosphorylation by a time-resolved parallel reaction monitoring mass spectrometry (PRM-MS) assay (data file S9). Nine of the 19 tested peptides showed increased phosphorylation over time (Fig. 4D). Among the underlying proteins were the transcriptional regulator SAMD4B (Ser^{592}); the nucleotide exchange factor TRIO (Ser^{2477}), which controls the activities of the GTPases RHO and RAC1; the RNA-editing enzyme ADAR (Thr^{601}); and USP10 (Thr^{74}), a ubiquitin hydrolase that removes ubiquitin from target proteins such as the tumor-suppressive transcription factor p53 and the ion channel CFTR (*29*, *30*). In addition, for some of the MAPK1/3 substrates [the cytoskeleton-associating SPECC1L Ser^{868}, the transcriptional repressor TSC22D4 Ser^{279}, ADAR Thr^{601}, and the lysine demethylase PHF2 Ser^{625}], several studies report dependency on the activation state of the MAPK pathway (*10*, *31*, *32*), and our kinase assays provided direct evidence that MAPK1/3 can be the phosphorylating kinase.

STRING protein interaction analysis of the 196 proteins underlying the KRAS core signaling signature revealed that about half of the proteins were not connected to each other or to KRAS (fig. S9D). However, our data strongly implied that they are indeed connected to the KRAS network. Many of these phosphoproteins have diverse or poorly characterized functions, suggesting that KRAS signaling extends far beyond well-researched biology and that such new avenues may be discovered on the basis of the data provided here. Functional enrichment analysis of the same proteins highlighted seven categories comprised of 106 proteins (Fig. 4E; data file S7). Expectedly, these included members of the MAPK pathway such as MAPK1/3 (p-Tyr^{187}/p-Tyr^{204}), the phosphatase DUSP16 (p-Ser^{501}), and the kinase ARAF (p-Thr^{181}) as well as the receptor tyrosine kinases (RTKs) EGFR (p-Thr^{693}), ERBB2 (p-Thr^{701}, p-Ser^{1054}), and EPHA2 (p-Ser^{901}). The latter represent described feedback signaling that is associated with resistance to KRAS inhibition (*33*–*35*). Important additional functional links could be established to Rho signaling, chromatin binding, mRNA binding, cadherin binding, mitotic cell cycle, and localization to the nucleolus. Hence, the short-term drug-induced phosphoproteome changes illuminated phenotypic drug responses long before they manifest visually under a microscope.

This was exemplified by changes in cell shape in response to sotorasib or MRTX1133 in MiaPaCa-2 or ASPC1 cells after 72 hours (Fig. 4F; fig. S10A,B; data file S2) which aligned with the observed abundance changes of phosphosites on several proteins involved in Rho signaling (*36*). Functional enrichment analysis also uncovered a link to the nucleolus, including altered amounts of phosphorylation of the cell proliferation marker MKI67 (p-Ser^{1533}) and its presumed interaction partner CCDC86 (p-Ser^{217})(*37*). Immuno-fluorescence microscopy data showed that KRAS inhibition led to the loss of MKI67 signal, indicating loss of nucleolar integrity, in MiaPaCa-2 and NCI-H23 cells (fig. S10C-E; data file S2). To investigate if CCDC86 Ser^{217} phosphorylation may be functionally important, we expressed GFP-tagged CCDC86 wild type (WT), S217A and S217D in NCI-H23 cells. Whereas cells expressing the WT or S217A forms of the protein showed no detectable phenotypic differences, expression of the phosphomimetic CCDC86 S217D disrupted nucleolar integrity in 25% of cells (Fig. 4G; fig. S10F,G; data file S2). The mechanism by which this occurs is currently not clear, but this very strong phenotype suggested that the phosphorylation status of CCDC86 Ser^{217} is of critical importance for nucleolar integrity and that this phosphosite is responsive to KRAS drugs.

Mutant KRAS activity dominates the signaling output of MEK and ERK

Several studies show that mutant KRAS still cycles between a GDP-bound (inactive) and a GTP-bound (active) state albeit at a much lower and mutation-specific rate than does WT KRAS (*38*–*41*). Such residual cycling is in line with the MoA of inhibitors that bind to the GDP-bound state of KRAS, such as adagrasib, which, over time, shifts the equilibrium from the GTP-bound to the GDP-bound state and thereby inhibits KRAS signaling. Given the parallel presence of HRAS and NRAS in cells and the evidence that KRAS can engage effectors beyond the RAF family (*42*, *43*), this provokes three important questions. First, to what extent does mutant KRAS lead to decoupling of the MAPK pathway from upstream signals provided by, for instance, receptor tyrosine kinases? Second, to what extent is inhibition of mutant KRAS alone sufficient for abrogating downstream MAPK signaling? Third, are there differences in the phosphoproteomes directly perturbed by KRAS or downstream MEK or ERK inhibition? To address these questions, we expanded decryptM profiling to inhibitors that act on targets upstream [SOS1, BI3406 (SOS1i); SHP2, RMC4630 (SHP2i)] or downstream [MEK, trametinib (MEKi); ERK, temuterkib (ERKi)] of KRAS (data file S1, data file S4). No selective inhibitors for HRAS or NRAS have yet been reported, which would have allowed probing their contributions directly.

Answering the questions above requires chemical probes that are highly selective for their targets. This was already established for the KRAS inhibitors. The decryptM profiles of RMC4630, BI3406, temuterkib, and trametinib showed bimodal pEC_{50} distributions implying off-target and/or off-pathway effects (fig. S11). The ability of decryptM profiling to recognize and account for such off-target and/or off-pathway effects highlighted the superiority of the concentration-response approach over traditional experiments using a fixed—and often arbitrarily high—drug concentration (fig. S12A-C, S13A). Kinase motif enrichment suggested, and Kinobead selectivity profiling confirmed, the kinases AAK1 (apparent dissociation constant, K_d^{app} 11 nM) and GAK (K_d^{app} 155 nM) as off-targets of temuterkib (fig. S13A-C; data file S7, data file S10). For trametinib, the kinase MKK6 (also called MAP2K6) has been reported as an off-target, but this protein did not score in published Kinobead assays, leaving the underlying cause of the second, low-potency distribution in NCI-H23 cells unresolved at this time (*1*, *44*). To ensure high quality of the subsequent analysis, phosphopeptides showing drug-induced

abundance changes were filtered such that they fall within the pEC_{50} distribution of KRAS core signaling signature members (Fig. 5A; fig. S12A-C).

Clustering the data of drug-perturbed phosphopeptides of all decryptM experiments separated the profiles of upstream inhibitors from those of KRAS and the downstream MEK and ERK inhibitors (Fig. 5B; fig. S14-S19). Unlike the KRAS and MEK inhibitors, SHP2 inhibition and, particularly SOS1 inhibition, did not lead to full abrogation of downstream MAPK3 (p-Tyr^{204}) activity in MiaPaCa-2 cells (Fig. 5C; fig. S20A). Particularly SOS1 inhibition showed only weak pathway engagement illustrated by the abundance changes of only few phosphopeptides in MiaPaCa-2 and none in ASPC1 cells (Fig. 5A). Consequently, cellular assays also showed that neither SHP2 nor SOS1 inhibition had a substantial effect on cellular growth (fig. S3; data file S2). Prolonged treatment with SHP2 and SOS1 inhibitors did not lead to increased MAPK pathway engagement either, excluding the possibility of kinetic drug effects (fig. S6B). Still, the observed abundance changes of several phosphopeptides from the KRAS core signature in MiaPaCa-2 (SOS1i and SHP2i) and ASPC1 (SHP2i) cells - albeit with weaker effect sizes compared to KRAS inhibition - indicated that the decoupling of KRAS downstream signaling from upstream signals was incomplete (fig. S11, boxplots; fig. S14-S19). This is exemplified by the concentration-dependent reduction of ADAR Thr^{601} phosphorylation, a member of the KRAS core signaling signature, in MiaPaCa-2 and ASPC1 cells (fig S20B). SOS1 is the best-described guanine nucleotide exchange factor (GEF) for KRAS. Yet, the stronger phosphoproteomic response to SHP2 inhibition compared to SOS1 inhibition implied the presence of one or several alternative functional GEFs that are controlled by SHP2 activity and channel signals into the RAS-MEK-ERK axis (*45*, *46*). Several such candidates were expressed in the two cell lines (fig. S20C) but it is currently not clear whether any of these may play a role in this context.

In contrast to SOS1 and SHP2 inhibition, KRAS or MEK inhibition elicited qualitatively and quantitatively highly consistent phosphoproteome responses in MiaPaCa-2, NCI-H23, and ASPC1 cells (90.4%, 87.4%, and 91.8%, respectively; Fig. 5C,D, fig. S14-S19, fig S20D). Similarly strong consistencies were observed when comparing KRAS and ERK inhibition (81.8% in MiaPaCa-2 and 89.9% in ASPC1; fig. S14-S19). In line with this, we observed comparable effects on cell viability among KRAS, MEK and ERK inhibitiors (fig. S3; data file S2). When focusing on phosphorylation events that clearly responded to KRAS inhibition but not to MEK or ERK inhibition, we observed that there were not many (77 phosphopeptides) and that fewer still (4 phosphopeptides) were consistently regulated across cell lines (Fig. S20D,E). None of these phosphopeptides provided for a clear connection to other reported KRAS effector pathways such as those mediated by phospholipase Cε (PLCε), phosphoinositide 3-kinase (PI3K), or the GTPase Ral, making it appear unlikely that these pathways were activated by KRAS in the mutant cell lines analyzed here.

Given that PI3K is one of the most studied direct effectors of KRAS, we examined phosphorylation regulation on members of the PI3K-AKT-mechanistic target of rapamycin (mTOR) pathway in more detail (Fig. S21A,B). Several phosphopeptides from proteins annotated to be members of PI3K-AKT-mTOR signaling (KEGG entries hsa04150 and hsa04151) were indeed affected by KRAS but, importantly, also by MEK and ERK inhibition. At the same time, key phosphorylation sites that are direct substrates of AKT (AKT1S1 Thr^{246}; TSC2 Ser^{939}) or mTOR (AKT1S1 Ser^{183}) remained unaffected (fig S21A,C) (*47*, *48*). This implied that the overall activity of these kinases, as well as that of PI3K, was not substantially altered by KRAS, MEK, or ERK inhibition in the mutant KRAS cell lines studied here. To substantiate this interpretation, we compared our data to independently published decryptM data

using the PI3K inhibitor dactolisib (5), in which a very clear inhibition of these key phosphosites was indeed observed (fig. S21C).

In light of the above, the data supports the view that RAF is the major effector of mutant KRAS activity, that KRAS activity dominates the signaling output of the downstream kinases MEK and ERK, and that the cellular fate following KRAS inhibition is largely independent of the modality by which KRAS pathway inhibition is achieved in the cell lines tested.

Cell line–specific wiring of mutant KRAS signaling

The remarkable consistency of phosphoproteome responses between KRAS vs. MEK and KRAS vs. ERK inhibition not only applied to the KRAS core signaling signature but also included many more phosphopeptides within a particular cell line. As a result, the mutant KRAS-controlled signaling network may extend beyond 800 potential members in MiaPaCa-2 cells, 700 in NCI-H23 cells, and 1,900 in ASPC1 cells (fig. S22A; data file S8). At the same time, comparing decryptM profiles between cell lines showed that the response of the same phosphopeptide to inhibition of the same target protein can be very different. This was evident from comparing the responses induced by the same drug but in different cell lines. For instance, consistency for KRAS or MEK inhibition in ASPC1 vs. MiaPaCa-2 cells (51.6% and 53.1% respectively) was much lower than for KRAS vs. MEK inhibition in MiaPaCa-2 and ASPC1 cells (> 90%; Fig. 5B,D; fig. S14-S19). ASPC1 cells exhibited a particularly distinct response to KRAS, MEK, or ERK inhibition, and many phosphopeptides showed consistent drug-induced abundance changes for all three drugs. At the same time, several drug-regulated phosphopeptides were consistently observed in one cell line but were never even detected in any other cell line, indicating that these phosphorylation sites might only be present in specific cell lines (fig. S22B). Conversely, we observed abundance changes of many phosphopeptides in ASPC1 cells but not in any other cell line despite the fact that they were detected (Fig. 5E).

Functional enrichment analysis of the proteins underlying the drug-regulated phosphopeptides performed separately for each cell line treated with KRAS inhibitors highlighted biological functions already found for the KRAS core signaling signature (data file S7). For instance, Rho signaling was independently enriched in the data of all three cell lines, but a particularly large number of phosphopeptides on related proteins were identified in ASPC1 cells, suggesting a stronger connection between KRAS signaling and actin cytoskeleton dynamics in ASPC1 compared to the other cell lines (fig. S22C). In addition, the top 15 kinase motifs were enriched similarly in each cell line even though the underlying phosphopeptides were not necessarily the same (mainly MAPK and RPS6KA/B motifs) (fig. S22D, data file S7). In line with this, and despite substantial differences in the absolute number of phosphopeptides showing abundance changes, the proportion of proline-directed motifs (SP/TP; associated with MAPKs) was similar between the cell lines (Fig. 5A). In light of this data, we propose that although the same underlying molecular mechanisms (inhibition of the RAS-MEK-ERK axis) drive the observed phosphoproteomic responses in each cell line, the specific architecture of the KRAS signaling network varies depending on the presence, abundance and activity of cell line–specific factors such as kinases, phosphatases, guanine nucleotide exchange factors, GTPase-activating proteins, and/or transcription factors (Fig. 5F).

Two-dimensional decryptM distinguishes immediate KRAS pathway inhibition from adaptive cellular responses

KRAS inhibition was cytostatic in all cell lines tested but did not induce cell death (fig. S3; fig. S10A-E). To shed light on the steps leading to this cellular adaptation, we added a kinetic component to decryptM profiling of sotorasib in MiaPaCa-2 cells (concentration-dependent phosphoproteome profiling at 1, 2, 8, and 16 hours). Between 271 and 401 phosphopeptides showed concentration-dependent changes during the first 8 hours, increasing to 1,075 after 16 hours (fig. S23A; data file S1; data file S4). We classified the 550 phosphopeptides that exhibited concentration-dependent responses at one or more time points and that were detected at all four time points, into four categories (Fig. 6A; data file S4; see Materials and Methods for details): The constant group (233 phosphopeptides) showed significant abundance changes at three or all four time points but always at 16 hours (for example, the activity-regulating p-Ser^{380} site on RPS6KA1), thus representing drivers of sustained drug response. The early group (51 phosphopeptides) responded at 1 hour, and/or 2 hours, and/or 8 hours but not at 16 hours, possibly representing initiators of cellular adaptation, exemplified by BRD3 p-Ser^{281}. For the sake of clarity, we combined these two groups to describe the immediate response of cells that was a direct consequence of KRAS inhibition. The intermediate group comprised 68 phosphopeptides that showed responses at 8 hours and 16 hours only, exemplified by the E3 ubiquitin ligase RNF168 p-Thr^{208}. The late group (198 phosphopeptides) showed response at 16 hours only and included the cell cycle regulator WEE1 (p-Thr^{190}). The two latter categories most likely represented the result of the adaptive response and were, therefore, combined. Furthermore, t-SNE analysis separated the immediate from the adaptive responses (Fig. 6B), and practically all phosphopeptides of the KRAS core signaling signature belonged to the immediate response group (Fig. 6C). This clear temporal distinction of drug-induced phosphopeptide abundance changes indicated that not all were the direct consequence of KRAS inhibition.

As one might expect, kinase motif enrichment analysis for the immediate response showed overrepresentation of ERK as well as members of the RSK family motifs (Fig. 6D; data file S7). This was consistent with the full inhibition of activation loop phosphorylation of MAPK3 (p-Tyr^{204}) at all time points (Fig. 6E). In contrast, the adaptive response enriched for motifs phosphorylated by the cell cycle–regulating kinases CDK1–CDK6 (Fig. 6D; data file S7). MAPKs and CDKs both phosphorylate SP/TP sites, and we observed a shift in the proportion of SP/TP-containing phosphopeptides with drug-induced abundance changes, rising from 48% at 1 hour to 55% at 2 hours and 8 hours and reaching 75% at 16 hours of treatment (fig. S23A). In parallel, we observed a decrease in protein abundance of Cyclin A (CCNA2; Fig. 6E, data file S5) and CDC20 (E3 ligase relevant for M-phase progression; Fig. 6F) as well increased protein abundance of the cell cycle inhibitor CDKN1B (p27; relevant for G0/G1, fig. S23B). This indicated that cells were exiting from the cell cycle in response to KRAS inhibition. Fluorescence-activated cell sorting (FACS) analysis of drug-treated MiaPaCa-2 (Fig. 6G) and NCI-H23 (fig. S23C) cells confirmed a decrease of cells in S- and G2-phase following 16 hours of drug treatment and a concomitant increase of cells in G1-phase (data file S2). Therefore, we conclude that many of the phosphorylation changes observed in the adaptive response were not direct consequences of RAS–MEK–ERK pathway inhibition but rather reflected a population shift caused by cell cycle arrest. The arrest is caused by reduced CDK4/6 activity, mediated, for example, by the upregulation of CDKN1B, and leads to a depletion of cells in the S–M phases (where CDK1–CDK3 are active), resulting in decreased substrate phosphorylation. Collectively, this also suggests that the phosphopeptides of the constant group are the functionally most

important triggers of the adaptive cellular response, which manifests as cells eventually exiting the cell cycle and entering a quiescent state, thus evading cell death.

Posttranslational protein modifications are the primary regulators of cellular adaptation to KRAS inhibition

Cells changing from a proliferative to a resting state need to attenuate many cellular processes in one concerted action, and many of these could be traced in the 2D-decryptM data. Only relatively few significant changes were observed at the protein level (22 after 8 hours; 80 after 16 hours, fig. S23D; data file S5) of the ~7,000 proteins monitored in the experiment even though the majority of cells had already arrested (Fig. 6G). Proteins that decreased in abundance included ~10 transcription factors (including MYC, JUN, FOSL1, and SOX9), implying reduction of target gene transcription as described previously (*49*), but without numerically large changes in protein amounts of their target genes (fig S23B). Several cell cycle–regulating proteins [including CCNA2 (Cyclin A2), CCNB1 (CyclinB1), CDC20, CDCA5, and UHRF1], and negative regulators of the RTK-MAPK signaling axis (such as SPRY1/2/4 and ERRFI1) were also reduced. Among the few proteins that showed a clear concentration-dependent increase in protein abundance were CDKN1B (p27), a CDK inhibitor, and AGO1, a key player in posttranscriptional gene silencing, which again highlighted the involvement of cell cycle arrest and a decrease in transcription.

Our data suggests that cellular adaptation to KRAS inhibition is primarily mediated by PTMs rather than by transcriptional regulation of protein abundance. For example, dozens of phosphopeptides from chromatin-modifying enzymes (Reactome HSA-3247509) and DNA repair proteins (Reactome HSA-73894) showed abundance changes in both the immediate and adaptive responses (fig. S23E, data file S7). The former included lysine acetyl transferases, methyltransferases, and demethylases – enzymes that control the state of chromatin activity. Similarly, loss of phosphorylation on proteins important for DNA repair (such as BRCA2 p-Ser^{93}, ATR p-Ser^{435} or TP53 p-Ser^{315}) likely reflected reduced requirements for DNA repair activity in nondividing cells. Many—and often large—changes in PTMs were also detected at all the steps that control proteostasis. Reduction in transcriptional activity leads to reduction of mRNA processing activity, and we observed phosphorylation abundance changes on several proteins associated with this process, such as NCBP1 (p-Thr^{21}) and THOC5 (p-Thr^{328}; Fig. 4E). Similarly, changes in phosphorylation were detected on proteins important for translation, such as EIF4G1 p-Ser^{1231} (Fig. 4E).

Given the critical role of the ubiquitin system for cellular proteostasis, we investigated the ubiquitylation status of the proteome in response to 6 and 24 hours of KRAS inhibition by sotorasib in MiaPaCa-2 cells. This analysis revealed ~800 ubiquitylated peptides (of 13,000 monitored; fig. S24A-C; data file S6) with dynamic abundance changes mostly independent of their protein levels (Fig. 6H,I). Moreover, we observed a concentration-dependent increase in ubiquitylation on UBA1 (for example, ubi-Lys^{802}, ubi-Lys^{528}, and ubi-Lys^{657}), one of only two ubiquitin-activating (E1) enzymes found in humans (Fig. 6J). The earliest changes occurred in the catalytically active adenylation domain (AAD) as well as the catalytically active SCCH domain responsible for thioester bond formation, and both are critical for ubiquitin activation (*50*). Both ubi-Lys^{528} and ubi-Lys^{635} are located inside the active sites of UBA1, and the latter is in close physical proximity to the critical cysteine residue required for enzymatic activity. It is, therefore, very tempting to speculate that this ubiquitylation leads to attenuation of enzymatic

activity. Similarly, increased ubiquitylation was also observed near the catalytic residues of several E2 enzymes as well as residues that mediate interactions with E1 and E3 enzymes (for example UBE2N, UBE2S, and UBE2L3; fig. S24D,E). Ubiquitylation near the catalytic residues has been reported to inactivate E2 enzyme activity in UBE2N and UBE2S (*51*, *52*).

Discussion

KRAS has long been considered a critical driver of many cancers, and the approval of sotorasib and adagrasib in 2021 and 2022, respectively, has expanded the therapeutic options for patients with KRAS G12C-mutated, locally advanced or metastatic non-small cell lung cancer (NSCLC). Unfortunately, neither inhibition nor degradation of mutant KRAS (*16*) kills cancer cells, and clinical studies combining KRAS-targeting drugs with inhibitors targeting up- or downstream proteins (including EGFR, SHP2, SOS1, MEK, and ERK) have also not achieved tumor cell eradication (NCT04975256, NCT04185883 (*53*)). Instead, following an initial period of disease stabilization, tumor cells often adapt and resume proliferation (*54*, *55*). This study aimed to shed new light on the molecular mechanisms leading to the initial antiproliferative effect by using the aforementioned inhibitors in multidimensional and fully concentration-resolved chemical proteomics experiments in three KRAS-mutant lung and pancreatic cancer cell lines.

The first important outcome of this work is the confirmation that KRAS inhibitors are highly selective for their target, which allows for using them as chemical probes to study mutant KRAS-dependent signaling. This, in turn, enabled discovering that mutant KRAS cancer cells possess a common KRAS core signaling signature that operates across all cell lines and includes many new phosphorylation sites and proteins not previously associated with KRAS signaling. The data also showed that this KRAS core signature is embedded in a cell line–specific KRAS network, members of which are not found in every cell line or do not respond in the same way to inhibitors. All data collected here were obtained from drug perturbations of only three G12C and G12D KRAS cell lines, but the presence of the KRAS core signaling signature could be confirmed in additional published phosphoproteome studies (*8*, *11*). Unfortunately, there are no equivalent studies for other KRAS-mutated models (for example. KRAS G12V/R), which is why we cannot state to what extent the functional relevance of the KRAS core signaling signature may also apply in these cases. Because inhibitors targeting a broader range of KRAS mutations continue to emerge, it will become increasingly feasible to validate the presence and functional importance of the KRAS signaling signature across other common mutational contexts.

A second noteworthy result is that mutant KRAS-mediated signaling does not appear to be fully decoupled from upstream signals, particularly from SHP2 and less so from SOS1. Although the degree of decoupling may vary across cell lines, the data collected for SHP2 and SOS1 inhibition implies that one or several other GEF proteins may be active in KRAS mutant cells. However, these residual upstream signals appear to have little impact on the overall output of the RAS-MEK-ERK signaling axis because KRAS or downstream inhibitors alone completely abrogate signaling and, therefore, result in the same phenotypic effects.

A third key finding is that the effects of KRAS and downstream inhibition were largely indistinguishable, suggesting that RAF acts as the primary effector of mutant KRAS in the cell lines studied. We found no evidence to support the direct involvement of mutant KRAS in the regulation of PI3K or other effector proteins. Abundance changes of certain phosphorylation sites on proteins that are annotated to be members of the PLCε or PI3K-AKT-mTOR pathways (NFATC3, CAMK1, RPS6KB1, GSK3B) were observed in response to KRAS, MEK, or ERK

inhibitors. This suggests either a feedback loop from ERK to PLCε or PI3K signaling components or a direct involvement of these proteins in the RAS-MEK-ERK axis. How MEK or ERK directly or indirectly accomplish this is currently not clear, but mining our data set may provide for valuable starting points for future work on this topic.

A fourth and important result was obtained from the two-dimensional (time- and concentration-dependent) decryptM experiments. The analysis enabled the separation of immediate RAS-MEK-ERK signaling in response to pharmacological inhibition from the consequence of cell cycle arrest. This provides further clarifications to a study by Klomp *et al.* on the ERK-regulated phosphoproteome (*11*) that reports a "[…] highly dynamic response of the kinome to KRAS-ERK inhibition […]," including changes in activity of several CDKs as a result of ERK inhibition. Our interpretation of the 2D decryptM data specifies that KRAS inhibition leads to inhibition of the G1/S checkpoint by way of losing CDK4/6 activity. The observed changes in the phosphoproteome at later time points are therefore merely a consequence of the depletion of cells in S and M phase and a concomitant increase of cells in G0/G1, rather than abrogation of CDK1-3 activity in direct response to KRAS inhibition. Such an interpretation would support a more general mechanism that explains why drug-treated cancer cells often show quiescent phenotypes when treated with signaling inhibitors (*56–58*).

The last and related major outcome is the observation that the antiproliferative effect of KRAS inhibition is initiated by the regulation of PTMs, leading to immediate consequences for proteostasis, eventual exit of cells from the cell cycle, and a subsequent accumulation of quiescent cells. Such a PTM-controlled transition may not only allow cells to avoid the energy costs associated with substantial changes to protein abundance through transcriptional remodeling, but may also enable cancer cells to return rapidly to a proliferative state when conditions improve. Several of these observations warrant further work in the future. For instance, it would be interesting to find out which transcription factors control the expression of proteins in amounts essential for cell growth and proliferation. Another exciting future aspect relates to the finding that E1 and E2 enzymes of the ubiquitin system are themselves ubiquitinylated near residues critical for catalytic activity in response to KRAS inhibition or the consequential exit from the cell cycle. Such modifications would be expected to inactivate enzymatic activity as a result of one (or several) ubiquitin moieties sterically blocking the active sites. The stoichiometry of these ubiquitylation events in response to KRAS inhibition is not known at present, but the observed fold-change in the UBA1 SCCH domain (ubi-Lys^{635}) was rather large (4-5-fold). Given that only two ubiquitin-activating E1 enzymes exist in humans, even small reductions in their enzymatic activity could have profound effects on the entire ubiquitin system of a cell and lead to rapid changes in proteostasis. There are reports in the literature on some of these ubiquitin sites that either interpret the ubiquitylation events to occur by 'random' E3 ligase activity or are the result of a controlled process to inhibit E1/E2 enzymatic activity (*51, 59*). Our data shows that these sites are dynamically regulated in a KRAS-targeting drug concentration–dependent fashion. This supports the view that attenuating the activity of E1 and E2 enzymes by modulating their ubiquitylation status could be another and (feedback) controlled step in the concerted action of cells in their transition from a proliferative to a quiescent state.

KRAS drug discovery is still in full swing, with numerous advanced molecules currently under development that target KRAS through diverse mechanisms. These include inhibitors that bind to the switch I/II regions in a mutation-specific manner but also pan-RAS inhibitors, molecular glues that form tri-complexes between KRAS-GTP and cyclophilin A to block effector

interactions, as well as KRAS degraders (*17*, *60*, *61*). It would be interesting to investigate how these molecules impact the phosphoproteomes of KRAS mutant cells. That said, and given the data in hand, we do not expect that the targetable KRAS nucleotide-bound state would make a strong difference to the immediate or adaptive response. This is because, in ASPC cells (G12D), the data obtained for MRTX1133 (dual KRAS on/off inhibitor) were highly similar to those obtained for MEK or ERK inhibition. Also, in the MiaPaCa-2 cells (G12C), effects of sotorasib, adagrasib, ARS-1620, and MRTX1257 (all KRAS off-inhibitors) were similar to MEK inhibition. In other words, MAPK pathway inhibition was effectively achieved by all these molecules. Hence, the cellular fate following KRAS inhibition appears to be rather independent of the exact modality of how KRAS inhibition is achieved. In line with this, recently reported KRAS degraders or KRAS (on) inhibitors also do not kill KRAS-mutant cells (*61*, *62*). The above suggests that mutant KRAS inhibition or degradation may have to be combined with drugs that prevent escape mechanisms, such as exit from the cell cycle, in order to kill the cancer cell. Targeting WEE1, PLK1, or CHK1 may be promising in this regard (*63*). The molecular resource created by the current study, which is available online for mining in ProteomicsDB (*20*) and in the form of interactive dashboards, may help scientists to identify further such vulnerabilities for future therapeutic exploitation.

Materials and Methods

If not specified otherwise, consumables were purchased from Sigma Aldrich, Sarstedt, Roth, Greiner, Marcherey-Nagel and Merck (table S1). For Proteomics sample workup and MS measurement only high purity grade consumables were utilized. A detailed list of other consumables and their respective vendors is provided in the Supplementary Materials under "Consumables List".

Culture conditions

MiaPaCa-2 and ASPC1 cells were cultured in DMEM/10% FBS. NCI-H23 cells were cultured in IMDM/10% FBS. Cells were maintained in a humidified incubator at 37°C with 5% CO_2. Cell lines were routinely inspected for mycoplasma contamination using PCR. Cell line authentication was accomplished by single nucleotide polymorphism (SNP) profiling (Multiplexion, Heidelberg, Germany).

Molecular biology and cloning

GFP–CCDC86 wt (*37*) was used to generate the GFP–CCDC86 S217A or GFP–CCDC86 S217D mutants, using the Q5® Site-Directed Mutagenesis Kit (New England Biolabs, Hitchin, UK) according to the manufacturer's protocol. For transient expression of GFP–CCDC86 wt, GFP–CCDC86 S217A or GFP–CCDC86 S217D constructs, NCI-H23 cells were seeded on coverslips into 6-well plates, transfected with 2µg of DNA using Polyplus JetPrime® (PEQLAB) and treated with DMSO (0.1%) or Sotorasib (300nM) for 24 hours.

Primers

S217_A_FW	5'-GCGAAAAGGTgctTCATCCCAGG-3'
S217_A/D_RV	5'-TTCTTTGCCCCGAAGCCG-3'
S217_D_FW	5'-GCGAAAAGGTgatTCATCCCAGGCC-3'

Fluorescence-activated cell sorting (FACS) for cell cycle analysis

For determination of cell cycle phase, DNA content was measured by flow cytometry. Cells were seeded in 6-well plate format and treated at ~40% confluence with the inhibitor Sotorasib at 300 nM for 1, 2, 8, 16, 24 and 36 hours or 0.1% DMSO as vehicle control for 24 hours, harvested and fixed in ice-cold 80% ethanol at -20°C overnight. The samples were stained with the PI/RNase staining buffer (BD Pharmingen) according to manufacturer's instructions and immediately measured by flow cytometry on a AccuriTM C6plus (Beckton Dickinson). The resulting data was analyzed using the Dean-Jett-Fox model of the cell cycle analysis platform provided by FlowJoTM v10.7.1 Software (BD Life Sciences).

Cell proliferation assay

Phenotypic effects after drug treatment on cell proliferation was evaluated after 72 hours of treatment duration with the AlamarBlue metabolic assay (Thermo Fisher Scientific). Cells were seeded into a 96-well microtiter plate (NCI-H23: 5000 cells/well, MiaPaCa-2: 2500 cells/well, ASPC1: 5000 cells/well) in triplicates and incubated at 37°C and 5% CO2. After 24 hours, inhibitor dilutions (see data file S2) were added including a vehicle control (0.1% DMSO). After a 72 h treatment, AlamarBlue reagent (Thermo Fisher Scientific) was added in a final concentration of 10% to each well and incubated for 5 hours at 37°C. The fluorescence was quantified at λex = 544 nm and λem = 584 nm on the microplate reader FluoStar Omega (BMG Labtech) and values were corrected for a blank value (medium only). Corrected values were normalized by the DMSO control. Data was analyzed with CurveCurator (v.0.5.0) by averaging all replicates and applying a non-linear regression analysis (four-parameter log-logistic regression) (*23*). For curve fitting, alpha-value value was set to 0.05, fc-value was set to 0 and curve fold changes were calculated relative to the control condition in accordance with CurveCurator's recommended workflow for cell viability data (control_fold_change = true) and interpolation was set to true. All CurveCurator related parameters are available on Zenodo.

Western blot analysis

Cells were treated at 70-80% (1-8 hour treatment) or ~40% (> 8 hour treatment) confluence with one fixed drug concentration for different time points and the control (0.1% DMSO). Cells were washed with PBS twice and lysed in lysis buffer (0.8% Igepal, 50 mM Tris-HCl pH 7.5, 5% glycerol, 1.5 mM $MgCl_2$, 150 mM NaCl, 1 mM Na_3VO_4, 25 mM NaF, 1 mM dithiothreitol (DTT) and supplemented with protease inhibitors (SigmaFast, Sigma) and phosphatase inhibitors (prepared in-house according to Phosphatase Inhibitor Cocktail 1, 2 and 3 from Sigma-Aldrich). Lysates were centrifuged at max. speed for 15 minutes at 4°C. Supernatants were collected and protein concentration was determined by Pierce Bradford assay (Thermo Fisher) according to the manufacturer's protocol. Equal protein amounts per sample (25-50 µg) were mixed 1:4 with Sample buffer (4x NuPAGE LDS Sample Buffer (Invitrogen), 100 mM DTT) and resolved on a NuPAGE 4-12% Bis-Tris gel. Proteins were transferred on polyvinylidene difluoride (PVDF) membranes. Membranes were blocked for 60 min in blocking solution (1x TBS-T + 5% BSA) and subsequently incubated with primary antibodies over night at 4°C. Anti-β-Actin (Santa cruz) and Anti-Phospho-p44/42 MAPK (Cell signaling technology) were used in a 1:500 and 1:2000 dilution as primary antibodies, respectively, following incubation with secondary antibody (IRDye® 680LT and 800CW, Licor) in a 1:10000 dilution for 2 hours at room temperature. Membranes were developed using an Odyssey imaging systems.

Cell morphology analysis

Bright light images were recorded using an IncuCyte S3 life cell imaging system (Essen Bioscience) at 37°C and 5% CO_2. The images were processed by ilastik, a supervised machine learning image analysis tool kit, in order to assign and quantify different categories of cell morphologies (*64*).

Immunofluorescence microscopy

Cells were fixed in 4% PFA and processed as previously described (*65*). Primary anti-Ki-67 was used in 1:100 dilution and secondary antibody was used in 1:500 dilution. Three-dimensional data sets were acquired using a wide-field microscope (DeltaVision) Cascade II:512 camera system (Photometrics) and Olympus UPlanSApo 100x/1.40na Oil Objective (Olympus). The data sets were deconvolved with the DeltaVision (SoftWoRx) software. Three-dimensional data sets were converted to maximum projection and exported as TIFF files.

Molecular docking simulation

Molecular docking simulation was conducted to obtain an overview about the interaction profile and possible binding mode of Adagrasib with the Elongation factor 1-alpha 2 (EEF1A2) using the information obtained from reactive cysteine profiling. For this purpose, the x-Ray crystal structure of the protein (PDB code: 8B6Z (*66*)) was retrieved from protein data bank (www.RCSB.org). The SMILES string for the compound adagrasib was retrieved from Pubchem and converted to explicit hydrogen string using RDkit in python 3.9. A 3D conformation of the structure was thereafter generated by the ETKDG method of Riniker and Landrum as implemented in Rdkit package using torsion angle preferences from the Cambridge Structural Database (CSD) (*67*). Meeko v.0.5 was used to assign atom types, checking protonation type, merging non-polar bonds and define rotatable bonds. The PDB structure of the protein was converted to PDBQT after removing non-protein elements and calculation of partial charges using AutoDockTools1.5.6. Based on the reactive cysteine profiling data Docking grid was centered at x=216.593, y=161.738, z=289.044 corresponding to ATOM S in the side chain of EEF1A2 Cys^{31} and the mentioned side chain was considered flexible during simulation. Docking was performed using the vina 1.2.5 python package with exhaustiveness set to 100 and number of generated poses was set to 100. After the docking run the distances between the enone moiety of adagrasib at different generated poses of the ligands in protein-ligand complexes with calculated affinity ≤ -6 kcal/mol (top 10% quantile range) were calculated. The structure in Figure 2D (after analyzing the obtained conformations of the top generated poses depicts a representative conformation of adagrasib and a probable binding mode for this structure.

Treatment and lysis for proteomics experiments

Cells were seeded in 10 cm dishes for phospho- and total proteome as well as ubiquitinome experiments and in 6-well format for reactive cysteine profiling and treated with drug dilutions (all drugs dissolved in DMSO, final concentration of DMSO was 0.1%) including a control (0.1% DMSO) (see data file S1 for detailed treatment conditions). Drug concentrations were chosen based on expected effect known from cell viability assays. . Medium (supplemented with 10% FBS) was changed prior to treatment. For phosphoproteomic, ubiquitinome and total protein analysis, cells were washed twice with PBS and subsequently lysed in 2% SDS lysis buffer (2% SDS, 10 mM Tris-HCl ph 7.5) and scraped off the plates. To hydrolyze the DNA and thereby reduce viscosity, the sample was boiled at 95°C for 10 min and trifluoroacetic acid (TFA) was added to a final concentration of 2%, incubated for 1-2 min at 95°C and subsequently

quenched with N-methylmorpholin (final concentration of 4%) to obtain a pH of 7.5-8. Samples were diluted 1:1 with lysis buffer. Protein concentration in cell lysate was determined using the Pierce™ BCA Protein Assay Kit (ThermoScientific) according to the manufacturer's protocol. For reactive cysteine profiling, treated cells were lysed (0.4% IGEPAL CA-630 in PBS with $MgCl_2$/$CaCl_2$, protease inhibitors (SigmaFast, Sigma) and 1x phosphatase inhibitors (prepared in-house according to Phosphatase Inhibitor Cocktail 1, 2 and 3 from Sigma-Aldrich)) on ice for 15 min and protein concentration was measured using Pierce™ Coomassie Plus. (ThermoScientific) according to the manufacturer's protocol.

Sample preparation for phosphoproteome and total protein analysis

Protein lysate was processed using SP3 sample workup. The beads suspension was prepared by mixing magnetic Sera-Mag-A (c = 50 mg/ml, Cytiva) and Sera-Mag-B (c = 50 mg/ml, Cytiva) beads in a ratio of 1:1, immobilized on a magnet and the supernatant was removed. Beads were washed twice with ddH_2O and then resuspended in ddH_2O in the original volume. A total of 200 µg per sample was mixed 1:7.5 (protein/beads weight) with the beads suspension and incubated for 10 min 1000 rpm RT. Proteins were precipitated by adding 100% ethanol to a final concentration of 70% and shaking for 10 min at 1250 rpm. The supernatant was removed on a magnet and beads were washed 3 times with 80% ethanol. Beads were washed with 100% ACN to remove residual ethanol. Proteins were reduced and alkylated in 100 µl Reduction and Alkylation buffer (100 mM EPPS/NaOH, pH 8.5, 55 mM CAA, 10 mM TCEP) for 1 h at 37°C and 1200 rpm. Proteins were digested o/n at 37°C and 1000 rpm by adding Trypsin 1:50 (trypsin/substrate weight) to each sample. Beads were immobilized on a magnet and supernatant containing the protein digest was collected, acidified with 1% TFA. The digest was desalted using HLB desalting plates (10 mg N-Vinylpyrrolidon-Divinylbenzol porous particles 30 µm, Macherey Nagel). Plates were equilibrated by 1000 µl solvent A (0.1% TFA, 1 min, 250 rpm). The digest was slowly loaded by gravity. Samples were washed with 1000 µl solvent A, peptides were eluted by gravity in 200 µl Solvent B (0.1% TFA, 70% ACN). Residual volume was collected via 2 min centrifugation at 200 rpm and a subsequent centrifugation step at 1000 rpm for 1 min. Peptides were freeze dried and stored at -20°C until further use. Desalted peptides were labelled with tandem mass tags 11 (TMT11)-plex (Thermo Scientific) as previously described (*68*) with small modifications. In brief, dried and cleaned peptides were reconstituted in 20 µl of 100 mM EPPS*NaOH (pH 8.5) buffer. 0.5 mg of TMT-11plex reagent was reconstituted in 16 µl water-free ACN to a working concentration of ~30 µg/µl. 5 µl of this TMT reagent solution was transferred to the peptides. The reaction was incubated at 25°C and 400 rpm for one hour, followed by quenching with 5 µl of 1.5% hydroxylamine. The TMT channels were then pooled together and acidified with formic acid (FA) to a final concentration of 1%. The reaction wells were washed with 25 µl washing solution (10% FA in 20% ACN) and added to the TMT pool. The TMT pools were dried down in the speed-vac and stored at -20°C. The peptide pool was reconstituted in 500 µl 0.1 % FA and desalted using C18 Sep-PAK cartridges (Waters Corp.; wash solvent: 0.1% FA; elution solvent: 0.1% FA in 50% ACN) according to the manufacturer's protocol following fractionation into 96 fractions using a Vanquish HPLC system (Thermo Fisher) equipped with a Waters XBridge BEH130 C18 3.5 µm 4.6 x 250 mm column (Solvent A: 25 mM ammonium bicarbonate (pH = 8.5), solvent B: 100 % H_2O, solvent C was 100 % ACN) using a linear gradient from 7% to 45% ACN in the constant presence of 2.5 mM ammonium bicarbonate. Sample was pooled to 48 fractions, acidified with formic acid to a final

concentration of 0.1%, and 10% of each fraction was collected and freeze dried for total proteome measurement. Remaining fractions were freeze dried and further used for enrichment of phosphorylated peptides via metal ion affinity chromatography (IMAC) on a AssayMAP® Fe(III)-NTA cartridges (Agilent) with the Bravo Agilent pipetting system following the Phosphopeptide Enrichment Protocol, included in the Agilent AssayMAP® Bravo® Protein Sample Prep Workbench v2.0 software suite. Briefly, the dried 48 TMT peptide fractions were reconstituted in 0.1% TFA 80% ACN and combined into 12 fractions (final volume of 200 µl per fraction). The AssayMAP® Fe(III)-NTA cartridges were equilibrated with 150 µl 0.1% TFA in 80% ACN. The TMT-pool peptide mix was loaded on the cartridges and the flow through was collected. After washing with 0.1% TFA in 80% ACN phosphorylated peptides were eluted with 60 µl of 1% ammonium hydroxide NH_4OH. The eluates were acidified up to 0.5% FA, dried down in the speed-vac, and stored at -20°C for MS analysis of the phosphoproteome.

Sample preparation for reactive cysteine profiling

Treated samples were lysed (0.4% IGEPAL CA-630 in PBS and Halt™ Protease Inhibitor Cocktail (Thermo Scientific) and processed as previously described, with slight modfications (*22*). Extracted proteins were incubated with 0.5 mM desthiobiotin iodoacetamide (DBIA) for 1 hour at room temperature. The reaction was quenched by adding 10 mM DTT for 30 min at room temperature and free cysteine residues were subsequently alkylated using 55 mM CAA for 30 min at room temperature. Protein amount was determined by Bradford Assay (Pierce™ Coomassie, Thermo Scientific) and from each condition 150 µg were further used for trypsin S-TRAP™ digestion (Protifi, USA). The overnight digestion was conducted according to the manufacturer´s protocol with a trypsin(Promega):protein ratio of 1:50 (trypsin/substrate weight). Resulting peptides were dried down and reconstituted in HEPES buffer (50 mM, pH 8.5). TMT (18-plex) labeling was performed as published before (*68*) using a 1:1 ratio of peptides and TMT reagent (wt:wt; Thermo Scientific). After TMT labeling, samples were pooled and desalted using SepPak column with the manufacturer´s protocol (Waters Corp.). Biotinylated sample were enriched using Streptavidin cartridges on a Bravo AssayMAP (both Agilent Technologies). In brief, cartridges were primed using 1% FA followed by an equilibration step using PBS. Samples were reconstituted in PBS and loaded onto the cartridges. After three washing cycles with water, bound peptides were eluted using 50% ACN and 0.1% TFA in water and further dried down. The enriched peptides were desalted and fractionated using StageTips (*69*). In brief, acidified samples were loaded onto StageTips (5 disks, Empore C18, Sigma), washed with 0.1% FA, and eluted into 6 fractions with an increasing concentration of ACN in 25 mM ammonium formiate. Fractions were dried down at stored at -20°C until acquisition on the mass spectrometer.

Sample preparation for ubiquitinome profiling

Lysate was processed with SP3 sample workup as described above using a 1:1 mix of magnetic Sera-Mag-A (c = 50 mg/ml, Cytiva) and Sera-Mag-B (c = 50 mg/ml, Cytiva) beads. A total of 600 µg per sample was mixed 1:7.5 (protein/beads weight) with the beads suspension and incubated for 10 min 1000 rpm RT. Proteins were precipitated by adding 100% ethanol to a final concentration of 70% and shaking for 10 min at 1250 rpm. The supernatant was removed on a

magnet and beads were washed 3 times with 80% Ethanol. Beads were washed with 100% ACN to remove residual ethanol. Proteins were reduced and alkylated in 100 µl RA buffer (100 mM EPPS/NaOH, pH 8.5, 55 mM CAA, 10 mM TCEP) for 1 hour at 37°C and 1200 rpm. Proteins were digested o/n at 37°C and 1000 rpm by adding Trypsin 1:50 (trypsin/substrate weight) to each sample. Beads were immobilized on a magnet and supernatant containing the protein digest was collected, acidified with 1% TFA and separated samples were pooled accordingly. The digest was desalted using HLB desalting plates (10 mg N-Vinylpyrrolidon-Divinylbenzol porous particles 30 µm). Plates were equilibrated by 1000 µl solvent A (0.1% TFA, 1 min, 250 rpm). The digest was slowly loaded by gravity. Samples were washed with 1000 µl solvent A, peptides were eluted by gravity in 200 µl Solvent B (0.1% TFA, 70% ACN). Residual volume was collected via 2 min centrifugation at 200 rpm and a subsequent centrifugation step at 1000 rpm for 1 min. Peptides were freeze dried and stored at -20°C until further use. For ubiquitinome analysis the previously published protocol from Udeshi et al. was used with modification (*70*). The PTM-Scan ubiquitin remnant motif (K-ε-GG) kit (Cell Signaling Technology, Kit #5562) was crosslinked. For each enrichment from desalted peptides (per sample), one-eighth of a vial of crosslinked antibody (~31.2 µg) were used. Briefly, antibody-bound beads were washed three times with 100 mM sodium borate (pH 8.8) and incubated with 20 mM DMP (in 100 mM Borax, pH 8.8) for 30 min at room temperature (RT). After each wash, the antibody beads were centrifuged at 2000 g for 1 min, allowed to settle on ice for 30 s, and the supernatant was removed. Subsequently, the beads were washed twice with 200 mM ethanolamine (pH 8.0) and incubated overnight at 4 °C in the same buffer. Following this incubation, the beads were washed three times with immunoprecipitation (IAP) buffer (50 mM MOPS, pH 7.2, 10 mM sodium phosphate, 50 mM NaCl) and resuspended in IAP buffer. Peptides were reconstituted in 1 ml IAP buffer, centrifuged at 21,000 g at 4°C for 10 min, and transferred to a tube containing aliquoted antibody. The mixture was incubated at 4°C with end-over-end rotation at 20 rpm for 2 h. After incubation, the samples were centrifuged at 2000 g for 1 min, and the supernatant (IP flowthrough) was removed. The antibody beads were washed twice with 1 ml of ice-cold PBS buffer, resuspended in 47.5 µl of 100 mM EPPS (pH 8.5) for TMT labeling. 0.5 mg of TMT-11plex reagent (Thermo Scientific) were reconstituted in 12.5 µl waterfree ACN 2.5 µl TMT reagents (100 µg) were added to the bead suspension. The samples were spun down quickly and incubated at RT for 10 min at 1100 rpm. Quenching of the TMT labeling reaction was performed by adding 2 µl of 5% hydroxylamine to each sample, spinning down quickly, and incubating samples at RT for 5 min at 1100 rpm. Following quenching, samples were washed with 1 ml of ice-cold PBS buffer. Next, 120 µl of ice-cold PBS buffer was added to each tube to resuspend the antibody beads. All antibody beads from each tube were combined in a new 1.5 ml tube. The empty tubes previously containing antibody beads were washed once with 120 µl of ice-cold PBS buffer and added to the combined beads. The combined antibody beads were washed twice with 1 ml of ice-cold PBS. The final wash buffer was removed, and peptides were eluted by adding 100 µl of 0.15% TFA to the beads and incubating at RT for 5 min at 1100 rpm. The sample was spun down at 2000 g for 1 min, and the supernatant containing the eluted peptides was transferred to a new tube. The elution was repeated one more time, and the supernatant was added to the eluate from the previous step. The combined eluted peptides were fractionated as described before (*69*) with slight modifications using a StageTip packed with 10 layers of Empore C18 (3M) punches, preconditioned and equilibrated with 250 µl of ACN, followed by 250 µl of 50% ACN/0.1% FA, and 250 µl of 0.1% FA. Samples were loaded onto the StageTip and washed with 250 µl of 0.1% FA, and peptides were sequentially eluted with 40 µl of 0%, 5%, 10%, 15%, 20%, and 50% ACN in 25 mM ammonium formate (pH 10). The first and last fractions were combined, as were the second and fourth fractions, resulting in a total of four

fractions. The peptides were dried in a speed-vac and stored at -20°C for subsequent MS analysis of the ubiquitinome.

Kinobead affinity pulldown sample preparation

Kinobeads pulldown experiments were performed as previously described(*1, 71*). Briefly, cells were cultured as described above. The NCI-H23, ASPC1 and MiaPaCa-2 cells were lysed in 0.8 % IGEPAL, 50 mM Tris-HCl pH 7.5, 5% glycerol, 1.5 mM $MgCl_2$, 150 mM NaCl, 1 mM Na_3VO_4, 25 mM NaF, 1 mM DTT, protease inhibitors (SigmaFast, Sigma) and phosphatase inhibitors (prepared in-house according to Phosphatase inhibitor cocktail 1, 2 and 3 from Sigma-Aldrich). Cells were mixed 1:1:1 (according to cell count) and the total amount of protein was determined by a Bradford assay. Cell lysates (2.5 mg) were pre-incubated with increasing compound concentrations (DMSO vehicle, 1 nM, 3 nM, 10 nM, 30 nM, 100 nM, 300 nM, 1 µM, 3 µM, 30 µM) for 45 min at 4°C in an end-over-end shaker. Subsequently lysates were incubated with Kinobeads (17 µL settled beads) for 30 min at 4°C. The beads were washed and bound proteins were reduced with 50 mM DTT in 8 M Urea, 40 mM Tris HCl (pH 7.4) for 30 min at room temperature. After alkylation with 55 mM CAA proteins were digested with trypsin over night at 37 °C. Peptides were desalted and concentrated using SepPak tC18 µEluation plates (Waters) and dried down in a SpeedVac.

In vitro ERK2/MAPK1 assay

Synthetic peptides were synthesized as SpikeTides (JPT Peptide Technologies GmbH; data file S9). Peptide selections were based on results of DDA measurements of the deep phosphoproteome. Peptides were designed as 15-mers with serine or threonine in the central position, except when insufficient amino acids were present in the protein sequence (16-mers), with a C–terminal amide group and an acetylated N-terminus. A mutant version was designed for peptides harboring other potential phosphorylation sites (STY) within the sequence. JPT peptide (dissolved in 10% DMSO) were pooled (~300 pmol/µl) and further diluted in reaction buffer (120 mM HEPES pH 7.5, 6 mM $MgCl_2$, 6 mM $MnCl_2$, 1 mM DTT and 2 mM ATP) to reach a concentration of 6 µM. 10% of the reaction was removed as negative control. The reactions were initiated by adding enzyme to the substrate mix (30 nM enzyme, 1:200 enzyme/substrate) and incubated at 30°C and 600 rpm for 0, 5, 15, 30, 60, 90, 120 and 180 min. A control mix without addition of enzyme was sampled first. For each time point, 10% of the initial starting Volume was separated and reaction was quenched by adding FA to a final concentration of 1% and stored on ice. Each sample was desalted via StageTips (5 layers, diameter 1.5 mm C18 material, 3M Empore^{TM}). In brief, C18 material were self-packed into a 200 µl pipette tip and equilibrated by 0.1% FA. Peptides were loaded, washed with 0.1% FA and eluted using 80 µl 0.1% FA in 40% ACN. Desalted samples were further dried and used for MS measurements.

Total proteome LC-MS measurement

For total proteome measurement**,** peptides were measured with a Orbitrap Fusion Lumos or Eclipse Tribrid mass spectrometer (Thermo Scientific) that was coupled to a Vanquish microflow pump (Thermo Scientific). Samples were directly injected onto the Acclaim PepMap 100 C18 column (2 µm particle size, 1 mm ID × 150 mm) and peptides were separated at 50 µl/min using 25 min linear gradient from 4% to 32% LC buffer B (0.1% FA, 3% DMSO in ACN) in LC buffer A (0.1% FA, 3% DMSO). The MS was operated in a fast, data-dependent MS3-mode in positive polarity. The spray voltage was set to 3.5 kV supported by sheath gas (32 units) and aux gas (5 units) with a vaporizer temperature of 125 °C. The Cycle time was set to 1.2 s. MS1 spectra were acquired in positive mode in the Orbitrap with 60,000 resolution and a scan range from 360-1600 m/z (automatic gain control (AGC) target of 4e5 charges, maximum injection time (maxIT) of 50 ms). The isolated precursors were fragmented using HCD (collision induced dissociation, NCE 32%) and the resulting MS2 spectra were recorded in the ion trap operated in rapid mode, quadrupole isolation window was set to 0.6 Th, an AGC target of 3e4 charges, and a maxIT of 40 ms. For the subsequent SPS-MS3 scans, 8 MS2 fragments were selected simultaneously and further fragmented using HCD (NCE 55%). The resulting ions were recorded with a MS3 scan in the Orbitrap with 50,000 resolution, an AGC target of 1e5 charges, and a maxIT of 86 ms.

Phosphoproteomic LC-MS measurement

Enriched phosphorylated peptides were measured with an Orbitrap Eclipse Tribrid mass spectrometer (Thermo Scientific) coupled online to a Dionex Ultimate 3000 HPLC system (Thermo Scientific). After injection, the sample was transferred onto a trap column (75 µm x 2 cm) that was packed with 5 µm C18 resin (Reprosil PUR AQ - Dr. Maisch). Peptides were washed with the trap washing solvent (5 µl/min, 10 min) before conveying them to an analytical column (75 µm x 48 cm) that was packed with 3 µm C18 resin (Reprosil PUR AQ - Dr. Maisch). Peptides were separated using a stepped 80-minute gradient from 4 to 32% LC solvent B. Solvent A consisted of 0.1% FA and 5% DMSO in water. Solvent B consisted of 0.1% FA and 5% DMSO in ACN. The MS was operated in a sensitive, data-dependent MS3-mode in positive polarity. Peptides were ionized using a nano source with 2.0 kV spray voltage. Every 3 s, a full-scan (MS1) was recorded from 360 to 1800 m/z with a resolution of 60,000 in the Orbitrap in profile mode. The MS1 AGC target was set to 4e5, and the maxIT was set to 50 ms. Based on the full scans, precursors were targeted for MS2 scans if the charge was between 2 and 6. The MS2 quadrupole isolation window was set to 0.7 Th. Peptides were fragmentated by CID-targeting the precursor and the precursor-H_2PO_4 in parallel (multistage-activation) with a q-value of 0.25, 35% CE, and 10 ms activation time. The MS2 spectrum was acquired with 30,000 resolution, AGC target was set to 1.5e5 charges, the maxIT was set to 60 ms and a dynamic exclusion of 90 s. TMT reporter ions were measured in a MS3 scan based on the previous MS2 scan. Precursor ions were isolated with a charge stage-dependent MS3 quadrupole isolation window of 1.2 Th (z=2), 0.9 Th (z=3), 0.7 Th (z=4-6). The isolated precursor was then fragmented identically to the previous MS2 scan. The top 10 fragment ions of the MS2 scans were isolated in the ion trap in parallel (synchronous precursor selection) and fragmented using HCD (NCE 55%). The MS3 spectrum was acquired with 50,000 resolution from 100 to 1000 Th in the Orbitrap in centroid mode. The MS3 AGC target was set to 1e5 charges, and the maxIT was set to 120 ms.

LC-MS measurement of DBIA-modified peptides for reactive cysteine profiling

Enriched peptides were measured on an Orbitrap Eclipse Tribrid mass spectrometer (Thermo Scientific) coupled online to a Dionex Ultimate 3000 HPLC system (Thermo Scientific). After injection, the sample was transferred onto a trap column (75 µm x 2 cm) that was packed with 5 µm C18 resin (Reprosil PUR AQ - Dr. Maisch). Peptides were washed with the trap washing solvent (5 µl/min, 10 min) before conveying them to an analytical column (75 µm x 48 cm) that was packed with 3 µm C18 resin (Reprosil PUR AQ - Dr. Maisch). Peptides were separated using a three-step 100-minute linear gradient from 7 to 36% LC solvent B. Solvent A consisted of 0.1% FA and 5% DMSO in water. Solvent B consisted of 0.1% FA and 5% DMSO in ACN. The MS was operated in a sensitive, data-dependent MS3-mode in positive polarity. Peptides were ionized using a nano source with 2.0 kV spray voltage. Every 3 s, a full-scan (MS1) was recorded from 360 to 1800 m/z with a resolution of 60,000 in the Orbitrap in profile mode. The MS1 AGC target was set to 6e5, and the maxIT was set to 50 ms. Based on the full scans, precursors were targeted for MS2 scans if the charge was between 2 and 6. The MS2 quadrupole isolation window was set to 0.7 Th. Peptide fragmentation occurred in the linear ion trap by CID-targeting the precursor with a q-value of 0.25, 35% CE, and 10 ms activation time. The MS2 spectrum was acquired with 30,000 resolution, AGC target was set to 1.5e5 charges, the maxIT was set to 120 ms and a dynamic exclusion of 60 s. TMT reporter ions were measured in a consecutive MS3 scan based on the previous MS2 scan. Precursor ions were isolated with a charge stage-dependent MS3 quadrupole isolation window of 1.2 Th (z=2), 0.9 Th (z=3), 0.7 Th (z=4-6). The isolated precursor was then fragmented identically to the previous MS2 scan. The top 10 fragment ions of the MS2 scans were isolated in the ion trap in parallel (synchronous precursor selection). For the subsequent SPS-MS3 scans, ions were fragmented using HCD (NCE 55%). The MS3 spectrum was acquired with 50,000 resolution from 100 to 1000 Th in the Orbitrap in centroid mode. The MS3 AGC target was set to 1e5 charges, and the maxIT was set to 140 ms.

LC-MS measurement of ubiquitinome

Ubiquitinylated peptides were measured with an Orbitrap Eclipse Tribrid mass spectrometer (Thermo Scientific) coupled online to a Dionex Ultimate 3000 HPLC system (Thermo Scientific). After injection, the sample was transferred onto a trap column (75 µm x 2 cm) that was packed with 5 µm C18 resin (Reprosil PUR AQ - Dr. Maisch). Peptides were washed with the trap washing solvent (5 µl/min, 10 min) before conveying them to an analytical column (75 µm x 48 cm) that was packed with 3 µm C18 resin (Reprosil PUR AQ - Dr. Maisch). Peptides were separated using a stepped 90-minute linear gradient from 6 to 32% LC solvent B. Solvent A consisted of 0.1% FA and 5% DMSO in water. Solvent B consisted of 0.1% FA and 5% DMSO in ACN. The MS was operated in a sensitive, data-dependent MS3-mode in positive polarity. Peptides were ionized using a nano source with 2.0 kV spray voltage. Every 3 s, a full-scan (MS1) was recorded from 360 to 1800 m/z with a resolution of 60,000 in the Orbitrap in profile mode. The MS1 AGC target was set to 6e5, and the maxIT was set to 50 ms. Based on the full scans, precursors were targeted for MS2 scans if the charge was between 2 and 6. The MS2 quadrupole isolation window was set to 0.7 Th (charge states 3-6 were prioritized over charge state 2). Peptide fragmentation occurred in the linear ion trap by CID-targeting with a q-value of

0.25, 35% CE, and 10 ms activation time. The MS2 spectrum was acquired with 30,000 resolution, AGC target was set to 1.5e5 charges, the maxIT was set to 140 ms and a dynamic exclusion of 40 s. TMT reporter ions were measured in a consecutive MS3 scan based on the previous MS2 scan. Precursor ions were isolated with a quadrupole isolation window of 1.2 Th. The isolated precursor was then fragmented identically to the previous MS2 scan. The top 10 fragment ions of the MS2 scans were isolated in the ion trap in parallel (synchronous precursor selection). Fragment ions were fragmented using HCD (NCE 55%). The MS3 spectrum was acquired with 50,000 resolution from 100 to 1000 Th in the Orbitrap in centroid mode. The MS3 AGC target was set to 1e5 charges, and the maxIT was set to 120 ms.

LC-MS measurement of kinase affinity pulldowns

Peptides were analyzed using LC-MS/MS on a Dionex Ultimate3000 nano HPLC coupled online to an Orbitrap Fusion Lumos (Thermo Fisher Scientific) mass spectrometer. Peptides were delivered to a trap column (100 µm x 2 cm, packed in-house with Reprosil-Gold C18 ODS-3.5 µm resin, Dr. Maisch, Ammerbuch) and washed at a flow rate of 5 µl/min in solvent A0 (0.1% formic acid in water). Peptides were then separated on an analytical column (75 µm x 40 cm, packed in house with Rprosil-Gold C18 3 µm resin, Dr. Maisch, Ammerbuch) using a 52 min gradient ranging from 4-32% solvent B (0.1% formic acid, 5% DMSO in acetonitrile) in solvent A (0.1% formic acid, 5 % DMSO in HPLC grade water) at a flow rate of 300 nL/min. The mass spectrometer was operated in a data dependent mode, automatically switching between MS1 and MS2 spectra. MS1 spectra were acquired over a mass-to-charge ratio (m/z) range of 360-1300 m/z at a resolution of 60.000 (at m/z 200) in the Obitrap using a maximum injection time of 50 ms and an automatic gain control (AGC) target value of 4e5. Up to 12 peptide precursors were isolated (isolation width of 1.7 Th, maximum injection time of 75 ms, AGC value of 2e5), fragmented by HCD using 30% normalized collision energy (NCE) and analyzed in the Orbitrap at a resolution of 15,000. The dynamic exclusion duration of fragmented precursor ions was set to 30s.

Parallel reaction monitoring (PRM) of in vitro kinase assay

A parallel Reaction Monitoring (PRM) assay was developed based on the data-dependent acquisition (DDA) results of the in vitro kinase experiment. Targeted measurements using Parallel Reaction Monitoring (PRM) were performed with a 50-min linear gradient (4% to 32% acetonitrile) on a Dionex Ultimate 3000 RSLCnano system coupled to a Fusion Lumos Tribrid mass spectrometer (Thermo Fisher Scientific). The spectrometer was operated in PRM and positive ionization mode. MS1 spectra (360–1300 m/z) were recorded at a resolution of 120,000 using an AGC target value of 1×106 and a MaxIT of 50 ms. Targeted MS2 spectra were acquired at 60,000 resolution with a fixed first mass of 100 m/z, after HCD with 30% NCE, and using an AGC target value of 1×106, a MaxIT of 118 ms and an isolation window of 1.3 m/z.

Database search and analysis of PRM data from in vitro kinase assays

For analysis of PRM data from in vitro ERK2/MAPK1 kinase assays, a spectral library was generated from a MaxQuant (Version 1.6.12.0) search of all PRM generated raw files against a fasta file containing all synthesized JPT peptides. Parameters for MaxQuant with its built-in search engine Andromeda (*72, 73*) was set as follows: No proteolytic enzyme was specified. Phosphorylation of STY was used as variable modification. All other parameters were set to default. PRM data was analyzed using Skyline-daily (Version 22.2.0.351) (*74*). Peak integration, transition interferences and integration boundaries were reviewed manually, considering five to six transitions per peptide. The source table was exported and utilized for further analysis (available on Zenodo). Intensities of five to six fragment ions were summed up per precursor ion and used for quantification. For data analysis, filtering according to correlation of fragment ion intensities between sample peptides and library counterparts was applied ("Library Dot Product" (dotp) ≥0.85). The proteomics raw data, MaxQuant search results, used peptide sequence databases, and Skyline analysis files have been deposited to Panorama Public where they can be reviewed (see Data and Materials availability).

Database search of phosphoproteome, total proteome and ubiquitinome

MaxQuant (version 1.6.12.0) with its built-in search engine Andromeda (*72, 73*) was used for protein and peptide identification and quantification for ubiquitinome, phospho and total proteome analysis. MSMS spectra were searched against the human Swissprot reference list (canonical and isoforms, downloaded 2021/11/18). Unless stated otherwise, MaxQuant's default parameters were applied. Parameters were set as follows: Trypsin/P as the proteolytic enzyme with up to two missed cleavage sites allowed for total proteome measurements and four for phosphoproteome and ubiquitinome measurements; carbamidomethylation of cysteine as fixed modification, oxidation of methionine and N-terminal protein acetylation as variable modifications. A maximum of 5 modifications were allowed on peptides and the peptide length was set with a minimal length of 7 amino acids. Phosphorylation on serine, threonine, and tyrosine was allowed as variable modification specifically for the phosphoproteome (diagnostic peak for detection of the pY modification was removed from Maxquant default setting). Di-glycine on lysine (without additional new N-terminus) was added as a variable modification specifically for ubiquitinome data. Peptide spectrum match (PSM) FDR was set to 1% for all searches, while protein false discover rate (FDR) was set to 1% for total proteome analysis and 100 % for phospho-proteome and ubiquitinome analysis. Isotope impurities of the TMT batch were specified in the configuration of TMT modifications to allow MaxQuant the automated correction of TMT intensities (please refer to data file S1 for correction factor Lot Numbers). If not specified otherwise (please refer to data file S1), the evidence files from phosphoproteome datasets were submitted to SIMSI-Transfer (*75*) to reduce missing values in phospho peptide identification and quantification across individual experiment batches using a max_PEP of 1%. The p15 stringency cluster was used for further analysis, experiments were separated according to experiment names from the newly generated evidence.txt file after SIMSI transfer, experiments were separated into individual evidence.txt files and contaminants and reverse database hits were removed before further analysis.

Database search of data from reactive cysteine profiling

DBIA-modified peptides from the reactive cysteine profiling were analyzed using Proteome Discoverer (Version 2.5). Sequest HT was used as search engine. MSMS spectra were searched against the human Swissprot database (canonical and isoforms, downloaded 2021/11/18, supplemented with the KRAS G12C variant) as well as common contaminants (downloaded on 2021/05/21). DBIA (mass shift +296.185 Da) was manually included as variable modification of cysteines. Carbamidomethylation (C) and oxidation of methionine were allowed as further variable modifications. TMT-18plex was set as fixed modification of peptide N-termini and lysine. Trypsin/P was set as proteolytic enzyme with up to 2 missed cleavage sites allowed. Minimum peptide length was 6. Precursor and fragment mass tolerance were set to 10 ppm and 0.4 Da, respectively. Isotope impurities of the TMT batch were specified and correction of impurities was enabled (please refer to data file S1 for correction factor Lot Numbers). Quantification of reporter abundance were based on reporter intensity. Percolator was applied for FDR correction of PSMs with a target FDR (strict and relaxed) of 1%, while protein FDR was set to 100%. Peptides site localization probability threshold was set to 75%. Gene names for reactive cysteine data were added after exporting data from ProteomeDiscoverer (psm.txt) using R (packages AnnotationDbi and org.Hs.eg.db).

Database search of Kinase affinity pulldowns

Peptide and protein identification and quantification was performed using MaxQuant (v.1.6.3.3) with its built in search engine Andromeda (*72*, *73*) by searching the tandem MS data against all canonical protein sequences as annotated in the Swissprot reference database (canonical, downloaded 2018/11/28). Carbamidomethylated cysteine was set as fixed modification and phosphorylation of serine, threonine and tyrosine, oxidation of methionine and N-terminal protein acetylation as variable modifications. Trypsin/P was specified as the proteolytic enzyme and up to two missed cleavages were allowed. The minimum peptide length was set to seven and all data were adjusted to 1% PSM and 1% protein FDR. Label-free quantification and match between runs were enabled within MaxQuant (*76*).

Concentration-response curve fitting and statistics for concentration-response proteomic profiling

For phosphoproteome, ubiquitinome, total proteome and reactive cysteine profiling, CurveCurator (version 0.5.0, (*23*)) was used for fitting of concentration-response data using a 4 parameter sigmoidal model (Formula 1) for all raw search-engine data from concentration-response experiments. CurveCurator was also used for statistical evaluation (calculation of p-values; recalibrated F-statistic), following the relevance scoring approach as previously described (*23*). The following tables for different experimental data were submitted: evidence.txt from SIMSI or MaxQuant (for batches that were not subjected to SIMSI transfer) output for phosphoproteome and ubiquitinome data analysis; psm.txt from PD for reactive cysteine profiling; proteingroups.txt from MaxQuant for total proteome analysis. To define curve relevance, the alpha asymptote (p-value cutoff; alpha-value) was set to 0.05 for all data sets. The log2 curve fold change asymptote (fc-cutoff criteria; fc-value) was set to +/-0.45 (min. ratio ≈ 1.366) for phosphoproteome and ubiquitinome, +/-0.35 (min. ratio ≈ 1.27) for total proteome and

+/-0.6 (min. ratio ≈ 1.52) for reactive cysteine profiling. TMT channels exhibiting high noise levels were excluded from curve fitting and further analysis. If not stated otherwise (see data file S1), ratios were calculated against the DMSO (vehicle) control. Curves with more than 2 missing values were excluded from further analysis. Curve fold changes were calculated based on the regression model (Formula 1) as ratios between the highest and lowest concentration (according to CurveCurator; Formula 2).

Formula 1: $$f(x|\theta) = \frac{front-back}{1+10^{slope(x+pEC50)}} + back$$

θ: pEC_{50}, slope, front, back
x: log10 drug concentration

Formula 2: $$cfc = \frac{f(\max(x))}{f(\min(x))}$$

Further information about chosen drug treatment concentration range is provided in data file S1. All curve-related information generated by CurveCurator (EC_{50} values, p-values, log2 curve fold change etc.) was saved as curves.txt files per experiment. All experimental information (drug concentration, TMT channels, threshold values etc.) that was used as input information to execute CurveCurator are stored in respective TOML files. All information (including CurveCurator output, FDR estimates for each experiment etc.) is available for download on Zenodo. Additionally, all curves can be explored with the interactive HTML-based dashboard from CurveCurator (links provided on Zenodo). Of note, contaminants and reverse database hits were removed by CurveCurator (except for phosphoproteome data subjected to SIMSI transfer, which were removed manually). After curve-fitting, non-modified peptides (no phosphorylation of STY, no Gly-Gly (Ubi) of K, no Dbia of C) were removed from phosphoproteome, ubiquitinome and reactive cysteine profiling data sets.

For the kinobeads competition binding assays, protein intensities were normalized to the DMSO control and EC_{50} values were deduced by a four-parameter log-logistic regression using an internal pipeline that utilizes the drc; package in R (*77*). An apparent dissociation constant (K_d^{app}) was calculated by multiplying the estimated EC_{50} with a protein-dependent correction factor. The correction factor of a protein is defined as the ratio of the amount of protein captured from two consecutive pulldowns of the same DMSO control lysate.

Target annotation for reactive cysteine profiling and Kinobead data

For target annotation of reactive cysteine profiling, data obtained from automatic CurveCurator classification (“up”- or “down”, (*23*)) was manually curated (after initial statistical assessment by CurveCurator based on the relevance score approach (relevance score ≥ -log10(0.05)) using alpha-value and fc-cutoff criteria (see concentration-response curve fitting)). Classified cysteine-containing DBIA-modified peptides (cys-peptide; “down”) were manually curated based on their behavior across all experiments for reactive cysteine profiling. The KRAS G12D cell line treated with sotorasib and adagrasib served as a control to evaluate potential cellular effects; regulation of a cys-peptide across more than one cell line by a G12C inhibitor indicates a highly confident

target cysteine. A cysteine-containing peptide was considered a potential target if the resulting binding curve showed a sigmoidal curve shape with a concentration-dependent decrease. For kinobead pulldowns, targets of the compounds were annotated manually. A protein was considered a target if the resulting binding curve showed a sigmoidal curve shape with a concentration-dependent decrease of binding to the beads. Additionally, the number of unique peptides and MSMS counts per condition as well as the protein intensity in the DMSO control were taken into account. All concentration-response curve data can be explored in the files provided on Zenodo or MassIVE.

Classification of phosphoproteome, ubiquitinome and total proteome concentration-response data

CurveCurator automatically classifies concentration-response profiles into different categories. In brief, "up"- and "down"-regulation are based on the relevance score approach (relevance score ≥ -log10(0.05)) using alpha-value and fc-cutoff criteria (see concentration-response curve fitting). High confident "absence of regulation" profiles were additionally classified as "not" regulated curves (RMSE(mean model) ≤ 0.1). All other concentration-response profiles remained unclassified for two possible reasons: i) too high variance to be conclusive (p-value > 0.05). ii) low-variance with too small effect for regulation but too much of an effect to be classified as "not" regulated. For further details please refer to the original publication (*23*). Additionally, the data obtained from automatic CurveCurator classification was filtered to further decrease the false positives by the following rules: i) For all peptides or proteins to be classified as regulated, the EC_{50} value needed to fall within the second and second-to-last concentration points, thereby excluding data potentially influenced by outliers at the first or last concentration points. ii) Peptides or proteins with EC_{50} outside the second last concentration may result from not reaching the curve plateau at the last concentration and were therefore subjected to further scrutiny and classified as regulated if they met the following criteria: Phospho- and total proteome must have a root mean square error (RMSE) ≤ 0.09 to guarantee high representation of the data points by the curve. Ubiquitinome must have a root mean square error (RMSE) of ≤ 0.15 to ensure accurate representation of the data points by the curve. This threshold was increased due to the large number of up-regulated data points in the ubiquitinome dataset, which did not reach a plateau, leading to a higher likelihood of EC_{50} values falling outside the treatment range. All data (phosphoproteome, total proteome, ubiquitinome) must have an absolute log2 fold change of at least 0.6 of the curve fit at the second-to-last concentration point (Formula 1,2).
Peptides that did not meet these criteria were not considered as regulated and were therefore unclassified. Other classifications provided by CurveCurator, such as not-regulated or unclassified peptides, remained unchanged.

Site and protein annotation

Regulated sites and their sequence contexts were annotated by uploading peptide-level data tables (including those from reactive cysteine profiling, ubiquitinome, and phosphoproteome) to an in-house annotation tool (https://github.com/kusterlab/psite_annotation). The annotation was performed according to the authors guidelines, using a custom reference proteome (Swissprot,

downloaded 2021/11/18 for phosphoproteome and ubiquitinome; supplemented with KRAS G12C variant for reactive cysteine profiling).

General data analysis and visualization

For the visualization of reactive cysteine profiling data in Figure 2, all manually curated cys-peptides with abundance changes were displayed with pEC_{50} ($-\log10(EC_{50})$) values determined by CurveCurator. All other data were assigned a pEC_{50} ($-\log10(EC_{50})$) value of 3.5. Data that did not pass manual annotation ("down"; see target annotation for reactive cysteine profiling and Kinobead data) as well as cysteine-containing peptides with increasing responses ("up", implausible for competition based target deconvolution assays) were filtered from this analysis.

Concentration-response profiles of phosphoproteme, ubiquitinome and total proteome were grouped into a "high confidence" (all data with a p-value ≤ 0.05 or classified as "not" regulated, see curve classification) and "low confidence" (all unclassified data with p-values > 0.05) category to distinguish between high variance data ("low confidence") and data well-represented by the model ("high confidence", see fig. S2). This grouping was used for downstream analysis at the fold-change level to ensure the reliability of fold-change values. Analysis of phosphoproteome, ubiquitinome, and total proteome data that was analyzed using curve fold changes (e.g. Figure 3F), was exclusively performed on high confidence data only.

For visualization of concentration-response profiles from all proteomic data, the Null model provided by CurveCurator was used to display curves classified as "not" regulated (see curve classification) or "low confidence", while all other data were visualized using the corresponding dose-response model. For improved visualization, all proteomic concentration-response data presented in this manuscript was normalized to the lowest concentration (including curve fits, and data points) (Formula 3).

Formula 3 $$\tilde{y}_{corr} = \hat{y} \,/\, f(\min(x) \mid \theta)$$

$\hat{y}$: not-normalized y-values
$\tilde{y}_{corr}$: corrected y-values
$f(x \mid \theta)$: y-value at lowest concentration based on curve or Null model with parameters θ

For all analysis using the pEC50 dimension (e.g. Figure 3D), pEC_{50} ($-\log10(EC_{50})$) values were only used from concentration-response profiles that were classified as either "up" or "down" regulated according to all applied criteria (CurveCurator + outlier filter; see curve classification). Any additional filtering for downstream analysis of phosphoproteome data in fig S6C and fig. S11, S12 based on pEC50 dimension was exclusively performed on the pEC50s of regulated peptides. A detailed description of filtering steps can be found in the respective figures or below.

To quantify similarities between treatment conditions, we employed MAE (mean absolute error) or Jaccard index as similarity metrics. The mean absolute error (MAE) of log2 curve fold changes was used to quantify the overall agreement of effect sizes across conditions. In contrast, Jaccard similarity was used to assess whether the same sets of phospho-peptides were classified

as regulated across different treatments. This metric applied a binary classification (regulated vs. not regulated), irrespective of the magnitude of regulation. While MAE is sensitive to the overall magnitude of the concentration-response curves, it is less effective at pinpointing where differences originate. Jaccard similarity, on the other hand, can identify the overlap or divergence in the classification of peptides and focuses on the presence or absence of regulation rather than the effect sizes. For the calculation of the MAE for each pairwise comparison, identical peptides/proteins were included from two treatments for each comparison only if it was classified as up- or down- regulated in at least one of the two conditions and classified as "high confidence" concentration-response in both conditions. Based on all data points within a pairwise comparison, the mean absolute error was calculated on log2 curve fold changes (Formula 4).

Formula 4: $$MAE = \frac{1}{n}\sum_{i=1}^{n} | x_i - y_i |$$

n: number of observations
xi: value of x
yi: value of y

Jaccard similarity was calculated to quantify the overlap between binary classifications of phospho-peptides grouped by inhibitor category —specifically comparing sets of regulated concentration-response profiles, up-regulated versus not regulated, or down-regulated versus not regulated curves (Formula 5). Curves that were classified as not regulated in both conditions were excluded.

Formula 5: $$J(A,B) = \frac{|A_{up} \cap B_{up}| + |A_{down} \cap B_{down}|}{|A \cup B| - |A_{not} \cap B_{not}|}$$

A and *B*: sets of phospho-peptides classified as up/down regulated in two different conditions.

The cluster maps in Figure 3 and Figure 5 were generated using MAEs of log2 fold changes (see above) and were prepared with the R package 'heatmaply' employing Euclidean distance for clustering. Further R packages for data analysis included 'plotly', 'Rtsne', 'UpSetR'. Parts of the analysis including all pairwise comparisons between datasets (MAE or Jaccard similarity) can be found on Zenodo. A detailed description of individual analysis steps within this manuscript can be found below.

STRING network and functional enrichment analysis

For functional enrichment analysis and STRING network analysis, peptides were grouped according to their corresponding genes (canonical sequences of protein coding genes (Uniprot)). All genes associated with a peptide were included, except in cases where a peptide mapped to more than four genes, in which case it was excluded from the analysis. The STRING network was generated in Cytoscape (v. 3.9.1) using the STRING plugin (*78*). KRAS was manually

added to build the STRING network. The interaction score for the network was set to 0.7 (high confidence).
Functional enrichment analysis was performed in Cytoscape (v. 3.9.1) using STRING enrichment (provided by the STRING app) (*78*). The whole genome was used as background. To remove all STRING interactions, the confidence score was set to 1. Enrichment nodes were manually annotated using the q-values (adjusted p-values ≤ 0.05) provided by the tool (GO, Reactome, Wikipathway and Kegg pathway terms). For Figure 4E, all proteins underlying the KRAS core signature were used, for enrichment in fig. 22C, all proteins from phospho-peptides regulated upon different KRAS inhibitors (2 hours) were used, for fig. S23E all proteins from the immediate and adaptive response were used.

Kinase enrichment analysis

Kinase enrichment analysis was conducted specifically on down-regulated phospho-peptides, as most effects were observed in this category. The kinase enrichment tool based on the previously published kinase-substrate atlas provided on phosphosite.org was used with separate customized foreground and background data (*25*, *26*). For enrichment, the site sequence context of the phospho-peptides provided by he psite_annotation output (https://github.com/kusterlab/psite_annotation was truncated to ± 7 amino acids from the phospho-site at the central position. Foreground and background data was isolated based on the subset being analyzed (specified in the figure legend). The background data consisted of all sequences from the dataset from the experiment(s) under investigation. For example, when comparing effects of KRAS inhibition after 2 hours of treatment all site-sequence contexts from down-regulated phospho-peptides of KRAS inhibitor treatments after 2 hours were used for foreground dataset generation and all phospho-site sequence contexts were used for background data generation from the same experiments. Fisher enrichment analysis was performed with an enrichment threshold of 15. Statistical significant q-value threshold was set to 5 %. Of note, for visual representation of the kinase enrichment data, the axis was truncated at log2(enrichment factor) = 0, as kinases with log2(enrichment factor) < 0 did not reach statistical significance (p-value > 0.05).

Data comparison

Protein groups were extracted from different resources as follows: GAPs, GEFs, Phosphatases and Ubi-conjugating proteins were extracted by UniProt (*79*) keyword (GAP: uniprotkb_keyword_KW_0343, GEF: uniprotkb_keyword_KW_0344, Phosphatases: uniprotkb_keyword_KW_0904, Ubi: uniprotkb_keyword_KW_0833). Protein kinases were extracted from PFAM (PF00069). CDC25 homology containing GEFs (Ras guanine-nucleotide exchange factors catalytic domain) were extracted from PFAM/InterPro (IPR001895). Transcription factors were extracted from Lambert et al. (*80*). Phospho-site comparison between the ERK Compendium, Klomp et al., PSP regulatory and this study was performed on phospho-site level using the annotation provided by an internal pipeline (https://github.com/kusterlab/psite_annotation) but without annotated phospho-sites from isoforms. The ERK Compendium dataset was generated from Unal et al. (*8*). The Klomp et al. dataset was generated from adk0850_data_s3_differentialexpression tab 1 and tab 3 (*11*). The

PSP regulatory was downloaded from phosphosite.org. For comparisons only subsets of data were used (when possible) as specified in the figure legends. The Dactolisib and Refametinib datasets were extracted from Zecha et al. (*5*). The Maxquant output files (evidence.txt) were processed with CurveCurator (version 0.5) using parameters based on the authors recommendations for this dataset. Curve fits and related information are provided on Zenodo. PTM-Navigator was used to identify MAPK pathway membership (boxplots in Figure 3D) of regulated phospho-peptides (*81*). Phosphopeptides from proteins identified as members of MAPK pathway signaling (according to KEGG entry hsa04010) were extracted for analysis. Results are provided in data file S7. To determine phospho-peptides from proteins that are members of annotated PI3K-AKT-mTOR pathway (fig. S21), PTM Navigator was used to extract genes related to KEGG MAPK (hsa04010) pathway and KEGG PI3K-AKT-mTOR pathway (hsa04150, hsa04151; list provided on Zenodo). Peptides were grouped according to their corresponding gene (canonical sequences of protein coding genes (Uniprot)).

Reproducibility of the decryptM approach (fig. S4)

Reproducibility was evaluated using three biological replicates of a 2-hour Sotorasib treatment in MiaPaCa-2 cells (phosphoproteomes). For analysis at the potency level, pEC_{50} values were extracted from phospho-peptides that were identified and classified as regulated based on CurveCurator criteria and an additional outlier filter in all three experiments (see curve classification). Standard deviations (SDs) were calculated for pEC_{50} values, and coefficients of variation (CVs) were computed based on the corresponding EC_{50} values. To assess reproducibility of curve fold changes, all phospho-peptides that were detected across all three replicates, met the high-confidence criterion (see fig. S2, see general analysis), and were regulated in at least one condition (as defined above), were included. The CV of the curve fold change values was then calculated. Importantly, these three biological replicates were used exclusively for the reproducibility assessment. For all subsequent downstream analyses (including generation of KRAS core signaling signature), only a single replicate was used for simplicity. The specific replicate used in each chapter is indicated in data file S1 and data file S4.

Comparison of KRAS inhibitors for the delineation of pathway engagement (Fig. 3)

The apex of the pEC50 ($-\log10(EC_{50})$) distribution from regulated phospho-peptides in Figure 3D was determined for each treatment by calculating the local maximum of each individual pEC_{50} distribution. Regulated phospho-peptides with pEC_{50} values deviating by more than ±1 from the apex calculated for each treatment were not considered for further analysis (fig. S6A). This strategy was used as further quality criteria since phospho-peptides regulated by the same mechanism are considered to be regulated at similar concentrations (*5*). Pairwise comparisons were conducted between filtered regulated phospho-peptides from different treatments (fig. S7). Therefore, the fold-changes of same phospho-peptide from the two conditions was compared if the peptide was classified as regulated (after filtering) in at least one of the two conditions and met the “high confidence” criteria in the other condition to only compare fold changes from data with good curve fit representation of the data points (see general analysis; fig. S2). Mean absolute error (MAE) of log2 curve fold change values were calculated for all pairwise comparisons. All MAEs of log2 curve fold changes were subjected to hierarchical clustering to

identify similarities in drug effects (Fig. 3G, Formula 4). All comparisons between datasets can be found on Zenodo.

Identification of the KRAS core signaling signature (Fig. 4)

To identify the core KRAS signaling signature (Fig. 4A), only regulated phospho-peptides with pEC_{50} ($-\log10(EC_{50})$) values within ±1 from the apex of the pEC_{50} distribution from each treatment were selected as described before (Fig. 3D; fig. S6A). For each cell line, all phosphopeptides regulated by any of the KRAS inhibitors used were considered. All phospho-peptides falling within the pEC_{50} windows of the respective treatments (±1 from the apex) that were regulated in all three cell lines by at least one drug were assigned to the KRAS core signature. Additionally, phospho-peptides that were regulated in at least one, but not all, cell lines were included if they had a CurveCurator p-value ≤ 0.01, an absolute log2 fold change ≥ 0.6, and followed the same quality standards as regular curves (e.g. EC_{50} within the treatment range, see materials and methods (curve classification) for details).

Comparison of decryptM profiles of SHP2i, SOS1i, KRASi, ERKi and MEKi (Fig. 5)

To specifically analyze and compare KRAS pathway-related effects as a result of different inhibitors and minimize contributions from off-target or off-pathway signaling, phospho-proteomic data were filtered based on pEC_{50} ($-\log10(EC_{50})$) distributions (fig. S11; fig. S12). The rationale for this filtering step is that phospho-peptides regulated by the same cellular mechanism should show drug-regulation at similar concentrations(*5*). In detail, distributions for each treatment were manually inspected to identify unimodal or multimodal patterns. For unimodal distributions, KRAS pathway engagement was confirmed by the presence of regulated phospho-peptide from the KRAS core signature. The median pEC_{50} of these phospho-peptides was then calculated. In the absence of regulated KRAS core signature members, the treatment was considered ineffective in targeting the RAS-MEK-ERK axis and excluded from further analysis. For treatments with multimodal distributions, suggesting off-pathway and/or off-target effects, KRAS pathway engagement was evaluated same as described above for unimodal distributions (calculation of median of KRAS core member pEC_{50}). To identify drug-specific off-target signaling, regulated phospho-peptides were compared across all treatments within the same cell line, determining whether observed drug-regulated phospho-peptides potentially were specific to the drug under investigation. A phospho-peptide was considered to be potentially regulated in a drug-specific manner if the same phospho-peptide was classified at least once as "not" regulated and at the same time never classified as up- or down-regulated in other treatments within the same cell line. The pEC_{50} median of all drug-specific phospho-peptides was calculated for each treatment.
To focus on RAS-MEK-ERK axis-specific responses, only phospho-peptides with pEC_{50} values within ±1 of the KRAS core signature median were retained. In cases of bimodal distributions, peptides with pEC_{50} values within ±0.5 of the off-target median were excluded, even if they overlapped with the KRAS signature window. Although this filtering approach does not entirely eliminate off-pathway effects, particularly in cases of non-baseline-separated bimodal distributions, it qualitatively reduces the number of "interfering" phospho-peptides, thereby

improving the focus on RAS-MEK-ERK axis-driven effects. Only peptides passing this pEC_{50}-based filtering were used for downstream analyses.
Pairwise comparisons were conducted between filtered regulated phospho-peptides from different treatments (fig. S14-S19). Therefore, the fold-changes of same phospho-peptide from the two conditions was compared if the peptide was classified as regulated (after filtering) in at least one of the two conditions and met the "high confidence" criteria in the other condition to only compare fold changes from data with good curve fit representation of the data points (see general analysis; fig. S2). MAE of log2 curve fold change values were calculated for all pairwise comparisons (Formula 4). All MAEs of log2 curve fold changes were subjected to hierarchical clustering to identify similarities in drug effects (Fig. 5B). All comparisons between datasets can be found on Zenodo.
To determine the similarity of phosphoproteome responses between inhibitor categories, Jaccard similarity was calculated (Formula 5) using phospho-peptides with clear classifications ("up", "down", or "not" regulated; fig. S20). Only peptides classified as "up" or "down" (after filtering pEC_{50} distribution) in at least one condition were considered for comparison. Phospho-peptides were grouped by inhibitor class within each cell line, excluding those with inconsistent classifications across inhibitors within the same category (specifically KRAS inhibitors). Peptides unregulated in both conditions were excluded.
To investigate engagement of the PI3K-AKT-mTOR pathway under KRAS versus downstream inhibitor treatment (fig. S21), curated KEGG pathway sets (hsa04150 and hsa04151) were obtained via PTMNavigator. All phospho-peptides matching to proteins from these entries were selected if they met high-confidence criteria in both conditions (see fig. S2; see general analysis) and were classified as "up", "down", or "not" regulated in at least one treatment used for pairwise comparison. Known AKT- and mTOR-associated phospho-sites were annotated based on literature curation. The lollipop plot in fig. S21 contains PI3K-AKT-mTOR pathway related phospho-peptides across multiple treatments, and includes only phospho-peptides that were regulated in at least one condition and detected in both a KRAS inhibitor and at least one downstream inhibitor treatment.

Grouping of 2D decryptM experiments (Fig. 6)

For time-dose resolved data analysis, drug-regulated phospho-peptides (unimodal distributions) were filtered to follow the pEC_{50} ($-\log10(EC_{50})$) distribution of KRAS core signature members as described in figure S12. Only phospho-peptides identified across all four conditions, following the "high confidence" criterion in each (fig. S2, see general analysis) and regulated in at least one condition were considered for manual grouping into the four categories "early", "constant", "intermediate", "late". The constant group contains all phospho-peptides with significant abundance changes at three or all four time points but always at 16 hours. The early group contains all phospho-peptides that were significantly regulated at 1 hour, and/or 2 hours, and/or 8 hours but not at 16 hours. The constant and early group were combined to describe the immediate response. The intermediate group comprised phospho-peptides that showed responses at 8 hours and 16 hours only. The late group showed response at 16 hours. The intermediate and late group were combined to describe the adaptive response. Peptides that did not conform to any of these defined groups were excluded from further analysis, resulting in a curated set of 550 phospho-peptides. The absolute log2 fold changes of each peptide for all four curves was then

subjected to t-SNE analysis using the R package “RtSNE”. Grouped data is available on Zenodo and data file S4.

Comparison of ubiquitinome and total proteome (Fig. 6)

To investigate whether changes in the ubiquitinome are associated with changes in protein abundance, we compared the log2 curve fold changes between the regulated ubiquitin modified peptides from the ubiquitinome and their corresponding protein counterparts from total proteome. Therefore, regulated ubi-peptides were mapped to the corresponding UniProt identifiers in the total proteome dataset (16 hour Sotorasib treatment of MiaPaCa2). Only the canonical versions of protein-coding genes were used for mapping. If a ubi-peptide matched multiple protein groups, the log2 fold change of the protein group containing only the canonical version was used. If no such group existed, the log2 fold change of the protein group to which the peptide matched was used. Of note, we acknowledge that other Gly-Gly remnants may exist; however, ubiquitination is the most common modification associated with Gly-Gly signatures. Therefore, we refer to all Gly-Gly remnants as ubiquitination throughout the manuscript. All comparisons between datasets can be found on Zenodo.

Supplementary Materials
Figs. S1–S24.
Table S1.
Data files S1–S10.

References and Notes

1. S. Klaeger *et al.*, The target landscape of clinical kinase drugs. *Science* **358** (2017).
2. M. Frejno *et al.*, Proteome activity landscapes of tumor cell lines determine drug responses. *Nature Communications 2020 11:1* **11**, 1–12 (2020).
3. A. Lin *et al.*, Off-target toxicity is a common mechanism of action of cancer drugs undergoing clinical trials. *Science Translational Medicine* **11**, 8412 (2019).
4. M. Niepel *et al.*, Common and cell-type specific responses to anti-cancer drugs revealed by high throughput transcript profiling. *Nature Communications 2017 8:1* **8**, 1–11 (2017).
5. J. Zecha *et al.*, Decrypting drug actions and protein modifications by dose- and time-resolved proteomics. *Science* **380**, 93–101 (2023).
6. Y. C. Chang *et al.*, Decrypting lysine deacetylase inhibitor action and protein modifications by dose-resolved proteomics. *Cell Reports* **43**, 114272 (2024).
7. L. Litichevskiy *et al.*, A Library of Phosphoproteomic and Chromatin Signatures for Characterizing Cellular Responses to Drug Perturbations. *Cell Systems* **6**, 424-443.e7 (2018).
8. E. B. Ünal *et al.*, A compendium of ERK targets. *FEBS Letters* **591**, 2607–2615 (2017).
9. H. S. Solanki *et al.*, Cell-type Specific Adaptive Signaling Responses to KRASG12C inhibition. *Clinical cancer research : an official journal of the American Association for Cancer Research* **27**, 2533 (2021).
10. S. A. Stuart *et al.*, A Phosphoproteomic Comparison of B-RAF V600E and MKK1/2 Inhibitors in Melanoma Cells* □ S. *Molecular & Cellular Proteomics* **14**, 1599–1615 (2015).
11. J. E. Klomp *et al.*, Determining the ERK-regulated phosphoproteome driving KRAS-mutant cancer. *Science (New York, N.Y.)* **384**, eadk0850 (2024).
12. L. Huang *et al.*, KRAS mutation: from undruggable to druggable in cancer. *Signal Transduction and Targeted Therapy 2021 6:1* **6**, 1–20 (2021).
13. B. A. Lanman *et al.*, Discovery of a Covalent Inhibitor of KRASG12C (AMG 510) for the Treatment of Solid Tumors. *Journal of Medicinal Chemistry* **63**, 52–65 (2020).
14. J. B. Fell *et al.*, Identification of the Clinical Development Candidate MRTX849, a Covalent KRASG12CInhibitor for the Treatment of Cancer. *Journal of Medicinal Chemistry* **63**, 6679–6693 (2020).
15. J. Canon *et al.*, The clinical KRAS(G12C) inhibitor AMG 510 drives anti-tumour immunity. *Nature 2019 575:7781* **575**, 217–223 (2019).
16. J. Popow *et al.*, Targeting cancer with small-molecule pan-KRAS degraders. *Science* **385**, 1338–1347 (2024).
17. D. Kim *et al.*, Pan-KRAS inhibitor disables oncogenic signalling and tumour growth. *Nature 2023 619:7968* **619**, 160–166 (2023).
18. A. R. Moore *et al.*, RAS-targeted therapies: is the undruggable drugged? *Nature Reviews Drug Discovery 2020 19:8* **19**, 533–552 (2020).
19. M. Holderfield *et al.*, Concurrent inhibition of oncogenic and wild-type RAS-GTP for cancer therapy. *Nature 2024 629:8013* **629**, 919–926 (2024).
20. L. Lautenbacher *et al.*, ProteomicsDB: toward a FAIR open-source resource for life-science research. *Nucleic Acids Research* **50**, D1541–D1552 (2022).
21. S. Eckert *et al.*, Decrypting the molecular basis of cellular drug phenotypes by dose-resolved expression proteomics. *Nature Biotechnology 2024*, 1–10 (2024).
22. M. Kuljanin *et al.*, Reimagining high-throughput profiling of reactive cysteines for cell-based screening of large electrophile libraries. *Nature Biotechnology 2021 39:5* **39**, 630–641 (2021).
23. F. P. Bayer *et al.*, CurveCurator: a recalibrated F-statistic to assess, classify, and explore significance of dose–response curves. *Nature Communications* **14** (2023).
24. A. Noguchi *et al.*, Transcriptional regulation of ETV5 by mitogen-activated protein kinase via ETS-1 in human pancreatic cancer cells. *Scientific Reports 2025 15:1* **15**, 1–14 (2025).
25. J. L. Johnson *et al.*, An atlas of substrate specificities for the human serine/threonine kinome. *Nature* **613**, 759–766 (2023).
26. T. M. Yaron-Barir *et al.*, The intrinsic substrate specificity of the human tyrosine kinome. *Nature 2024 629:8014* **629**, 1174–1181 (2024).
27. R. Anjum *et al.*, The RSK family of kinases: emerging roles in cellular signalling. *Nature Reviews Molecular Cell Biology 2008 9:10* **9**, 747–758 (2008).

28. D. N. Sgouras *et al.*, ERF: an ETS domain protein with strong transcriptional repressor activity, can suppress ets-associated tumorigenesis and is regulated by phosphorylation during cell cycle and mitogenic stimulation. *The EMBO Journal* **14**, 4781–4793 (1995).
29. J. M. Bomberger *et al.*, The deubiquitinating enzyme USP10 regulates the post-endocytic sorting of cystic fibrosis transmembrane conductance regulator in airway epithelial cells. *The Journal of biological chemistry* **284**, 18778–18789 (2009).
30. J. Yuan *et al.*, USP10 regulates p53 localization and stability by deubiquitinating p53. *Cell* **140**, 384–396 (2010).
31. M. Courcelles *et al.*, Phosphoproteome dynamics reveal novel ERK1/2 MAP kinase substrates with broad spectrum of functions. *Molecular Systems Biology* **9**, 669 (2013).
32. C. Pan *et al.*, Global Effects of Kinase Inhibitors on Signaling Networks Revealed by Quantitative Phosphoproteomics. *Molecular & Cellular Proteomics : MCP* **8**, 2796 (2009).
33. M. B. Ryan *et al.*, Vertical pathway inhibition overcomes adaptive feedback resistance to KRASG12C inhibition. *Clinical cancer research : an official journal of the American Association for Cancer Research* **26**, 1633 (2020).
34. J. Y. Xue *et al.*, Rapid non-uniform adaptation to conformation-specific KRASG12C inhibition. *Nature* **577**, 421 (2020).
35. C. H. Chen *et al.*, MEK inhibitors induce Akt activation and drug resistance by suppressing negative feedback ERK-mediated HER2 phosphorylation at Thr701. *Molecular Oncology* **11**, 1273 (2017).
36. R. G. Hodge *et al.*, Regulating Rho GTPases and their regulators. *Nature Reviews Molecular Cell Biology 2016 17:8* **17**, 496–510 (2016).
37. K. Stamatiou *et al.*, CCDC86 is a novel Ki-67-interacting protein important for cell division. *Journal of Cell Science* **136** (2023).
38. R. J. Nichols *et al.*, RAS nucleotide cycling underlies the SHP2 phosphatase dependence of mutant BRAF-, NF1- and RAS-driven cancers. *Nature Cell Biology 2018 20:9* **20**, 1064–1073 (2018).
39. P. Bandaru *et al.*, Deconstruction of the Ras switching cycle through saturation mutagenesis. *eLife* **6**, e27810 (2017).
40. J. C. Hunter *et al.*, Biochemical and structural analysis of common cancer-associated KRAS mutations. *Molecular Cancer Research* **13**, 1325–1335 (2015).
41. S. R. Punekar *et al.*, The current state of the art and future trends in RAS-targeted cancer therapies. *Nature Reviews Clinical Oncology 2022 19:10* **19**, 637–655 (2022).
42. G. A. Repasky *et al.*, Renewing the conspiracy theory debate: does Raf function alone to mediate Ras oncogenesis? *Trends in Cell Biology* **14**, 639–647 (2004).
43. C. Kiel *et al.*, The Ins and Outs of RAS Effector Complexes. *Biomolecules* **11**, 1–29 (2021).
44. J. Basken *et al.*, Specificity of Phosphorylation Responses to Mitogen Activated Protein (MAP) Kinase Pathway Inhibitors in Melanoma Cells. *Molecular & Cellular Proteomics : MCP* **17**, 550 (2017).
45. E. Sheffels *et al.*, Oncogenic RAS isoforms show a hierarchical requirement for the guanine nucleotide exchange factor SOS2 to mediate cell transformation. *Science Signaling* **11**, 8371 (2018).
46. D. Vigil *et al.*, Ras superfamily GEFs and GAPs: validated and tractable targets for cancer therapy? *Nature Reviews Cancer 2010 10:12* **10**, 842–857 (2010).
47. B. D. Manning *et al.*, AKT/PKB Signaling: Navigating Downstream. *Cell* **129**, 1261–1274 (2007).
48. S. Battaglioni *et al.*, mTOR substrate phosphorylation in growth control. *Cell* **185**, 1814–1836 (2022).
49. J. A. Klomp *et al.*, Defining the KRAS- and ERK-dependent transcriptome in KRAS-mutant cancers. *Science (New York, N.Y.)* **384**, eadk0775 (2024).
50. Z. S. Hann *et al.*, Structural basis for adenylation and thioester bond formation in the ubiquitin E1. *Proceedings of the National Academy of Sciences of the United States of America* **116**, 15475–15484 (2019).
51. A. K. L. Liess *et al.*, Autoinhibition Mechanism of the Ubiquitin-Conjugating Enzyme UBE2S by Autoubiquitination. *Structure* **27**, 1195-1210.e7 (2019).
52. T. Takeuchi *et al.*, ISG15 modification of Ubc13 suppresses its ubiquitin-conjugating activity. *Biochemical and Biophysical Research Communications* **336**, 9–13 (2005).
53. H. Miyashita *et al.*, KRAS G12C inhibitor combination therapies: current evidence and challenge. *Frontiers in Oncology* **14**, 1380584 (2024).
54. J. Liu *et al.*, The KRAS-G12C inhibitor: activity and resistance. *Cancer Gene Therapy 2021 29:7* **29**, 875–878 (2021).
55. T. Isermann *et al.*, KRAS inhibitors: resistance drivers and combinatorial strategies. *Trends in Cancer* **11**, 91–116 (2025).
56. M. Osaki *et al.*, PI3K-Akt pathway: its functions and alterations in human cancer. *Apoptosis : an*

international journal on programmed cell death **9**, 667–676 (2004).
57. J. I. Kawada *et al.*, mTOR inhibitors induce cell-cycle arrest and inhibit tumor growth in Epstein-Barr virus-associated T and natural killer cell lymphoma cells. *Clinical Cancer Research* **20**, 5412–5422 (2014).
58. L. Jirmanova *et al.*, Differential contributions of ERK and PI3-kinase to the regulation of cyclin D1 expression and to the control of the G1/S transition in mouse embryonic stem cells. *Oncogene* **21**, 5515–5528 (2002).
59. G. Prus *et al.*, Global, site-resolved analysis of ubiquitylation occupancy and turnover rate reveals systems properties. doi: 10.1016/j.cell.2024.03.024 (2024).
60. C. J. Schulze *et al.*, Chemical remodeling of a cellular chaperone to target the active state of mutant KRAS. *Science* **381**, 794–799 (2023).
61. J. Popow *et al.*, Targeting cancer with small-molecule pan-KRAS degraders. *Science (New York, N.Y.)* **385**, 1338–1347 (2024).
62. P. Anastasiou *et al.*, Combining RAS(ON) G12C-selective inhibitor with SHP2 inhibition sensitises lung tumours to immune checkpoint blockade. *Nature Communications 2024 15:1* **15**, 1–17 (2024).
63. K. Fukuda *et al.*, Targeting WEE1 enhances the antitumor effect of KRAS-mutated non-small cell lung cancer harboring TP53 mutations. *Cell Reports Medicine* **5** (2024).
64. S. Berg *et al.*, ilastik: interactive machine learning for (bio)image analysis. *Nature Methods 2019 16:12* **16**, 1226–1232 (2019).
65. P. Vagnarelli *et al.*, Repo-Man Coordinates Chromosomal Reorganization with Nuclear Envelope Reassembly during Mitotic Exit. *Developmental Cell* **21**, 328–342 (2011).
66. M. Gemmer *et al.*, Visualization of translation and protein biogenesis at the ER membrane. *Nature 2023 614:7946* **614**, 160–167 (2023).
67. S. Riniker *et al.*, Better Informed Distance Geometry: Using What We Know to Improve Conformation Generation. *Journal of Chemical Information and Modeling* **55**, 2562–2574 (2015).
68. J. Zecha *et al.*, TMT Labeling for the Masses: A Robust and Cost-efficient, In-solution Labeling Approach. *Molecular & Cellular Proteomics* **18**, 1468–1478 (2019).
69. B. Ruprecht *et al.*, High pH Reversed-Phase Micro-Columns for Simple, Sensitive, and Efficient Fractionation of Proteome and (TMT labeled) Phosphoproteome Digests. *Methods in molecular biology (Clifton, N.J.)* **1550**, 83–98 (2017).
70. N. D. Udeshi *et al.*, Rapid and deep-scale ubiquitylation profiling for biology and translational research. *Nature Communications 2020 11:1* **11**, 1–11 (2020).
71. M. Reinecke *et al.*, Chemoproteomic Selectivity Profiling of PIKK and PI3K Kinase Inhibitors. *ACS Chemical Biology* **14**, 655–664 (2019).
72. J. Cox *et al.*, MaxQuant enables high peptide identification rates, individualized p.p.b.-range mass accuracies and proteome-wide protein quantification. *Nature Biotechnology 2008 26:12* **26**, 1367–1372 (2008).
73. J. Cox *et al.*, Andromeda: A peptide search engine integrated into the MaxQuant environment. *Journal of Proteome Research* **10**, 1794–1805 (2011).
74. B. MacLean *et al.*, Skyline: an open source document editor for creating and analyzing targeted proteomics experiments. *Bioinformatics* **26**, 966–968 (2010).
75. F. Hamood *et al.*, SIMSI-Transfer: Software-Assisted Reduction of Missing Values in Phosphoproteomic and Proteomic Isobaric Labeling Data Using Tandem Mass Spectrum Clustering. *Molecular & Cellular Proteomics* **21**, 100238 (2022).
76. J. Cox *et al.*, Accurate Proteome-wide Label-free Quantification by Delayed Normalization and Maximal Peptide Ratio Extraction, Termed MaxLFQ. *Molecular & Cellular Proteomics : MCP* **13**, 2513 (2014).
77. C. Ritz *et al.*, Dose-Response Analysis Using R. *PLOS ONE* **10**, e0146021 (2015).
78. N. T. Doncheva *et al.*, Cytoscape StringApp: Network Analysis and Visualization of Proteomics Data. *Journal of Proteome Research* **18**, 623–632 (2019).
79. A. Bateman *et al.*, UniProt: the universal protein knowledgebase in 2021. *Nucleic Acids Research* **49**, D480–D489 (2021).
80. S. A. Lambert *et al.*, The Human Transcription Factors. *Cell* **172**, 650–665 (2018).
81. J. Müller *et al.*, PTMNavigator: interactive visualization of differentially regulated post-translational modifications in cellular signaling pathways. *Nature Communications 2025 16:1* **16**, 1–16 (2025).
82. V. Sharma *et al.*, Panorama Public: A Public Repository for Quantitative Data Sets Processed in Skyline. *Molecular & Cellular Proteomics* **17**, 1239–1244 (2018).
83. J. Jumper *et al.*, Highly accurate protein structure prediction with AlphaFold. *Nature 2021 596:7873* **596**, 583–589 (2021).

84. Z. Lv *et al.*, Crystal structure of a human ubiquitin E1–ubiquitin complex reveals conserved functional elements essential for activity. *The Journal of Biological Chemistry* **293**, 18337 (2018).

Acknowledgments: We thank Kara Kreutz for contributions to sample processing, Karl Kramer for analysis of phenotypic data and OmicScouts for processing of the reactive cysteine profiling data. Parts of figures were created using BioRender.com.

Funding: This project has received funding from the European Research Council (ERC) under the European Union's Horizon 2020 research and innovation programme (grant agreement n° 833710). Work performed by the Kuster group was also supported by grants from the German Science Foundation (SFB1309; SFB1321) and the German Federal Ministry of Education and Research (BMBF; grant number 031L0305A). The Kuster and Bassermann labs are supported by the Deutsche Forschungsgemeinschaft (DFG, German Research foundation) – TRR 387/1 – 514894665. The Vagnarelli lab is supported by a Wellcome Trust Investigator award 210742/Z/18/Z to Paola Vagnarelli. K.S. was supported by a CHMLS PhD scholarship (Brunel University London).

Author contributions: NK, and BK conceived the study. N.K., K.S., YC.C., M.A., V.W., A.G., M.R., M.Ai., M.H., F.P.B. performed laboratory experiments. N.K., A.S., K.S., M.A., M.R. and B.K. performed data analysis. J.K., P.V., C.L., H.H., M.T., F.B. and B.K. directed and supervised experiments and data analysis. N.K. and B.K. wrote the manuscript with input from all authors.

Competing interests: B.K. is cofounder and shareholder of OmicScouts and MSAID. He has no operational role in either company. H.H. is cofounder, shareholder, and CEO of OmicScouts. J.K., M.R., and M.H. are present employees of OmicScouts. All other authors declare that they have no competing interests.

Data and materials availability:. The raw mass spectrometry proteomics data, protein. and peptide identification (search engine and SIMSI transfer outputs), Swiss-Prot reference database and quantification results, as well as concentration-response curves from CurveCurator or internal analysis pipelines used for Kinobeads analysis have been deposited with the ProteomeXchange Consortium via the MassIVE partner repository (https://massive.ucsd.edu/) with the dataset identifier PXD063604 (MassIVE identifier: MSV000097797). From these data, all analysis presented in this study can be reproduced. In addition, all concentration-response datasets including parameter TOML files, fitted curves saved as txt files and interactive dashboards can be viewed on Zenodo. Parts of the analysis can also be found on Zenodo (https://doi.org/10.5281/zenodo.15357873). The data are additionally also available in ProteomicsDB (https://www.proteomicsdb.org)(*20*). The mass spectrometry data and Skyline files for the PRM assays have been deposited to ProteomeXchange Consortium and the Panorama Public website (https://panoramaweb.org/2024_Kabella_KRAS.url; ProteomeXchange identifier PXD054509)(*82*). All other data needed to evaluate the conclusions in the paper are present in the paper or the Supplementary Materials. There are no restrictions on materials other than those imposed by the commercial availability of cell lines, antibodies, drugs, and other reagents used in this study.

Figure Legends

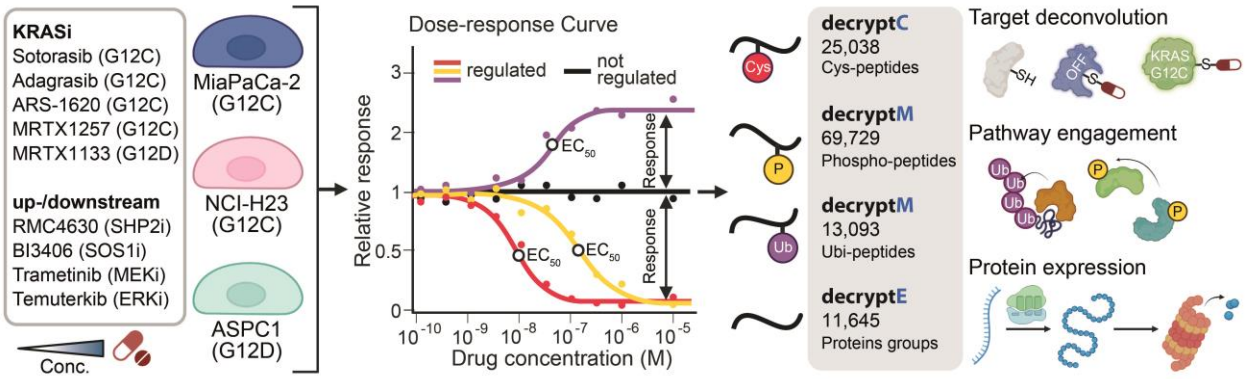

Fig. 1. Proteome-wide characterization of KRAS signaling inhibitors by concentration-response proteomics. Cells expressing different mutated KRAS proteins were treated with increasing concentrations of the indicated drugs, and the concentration-response profiles of reactive cysteines (Cys-peptides; for target deconvolution, decryptC), phosphopeptides and ubiquitylated peptides (for pathway engagement, decryptM), and proteins (for protein abundance, decryptE) were determined. Drug response (increased, decreased, or not changed relative to control) and potency (effective concentration to achieve 50% response, EC_{50}) were derived from fitted concentration-response curves followed by statistical assessment using CurveCurator (see Materials and Methods for details).

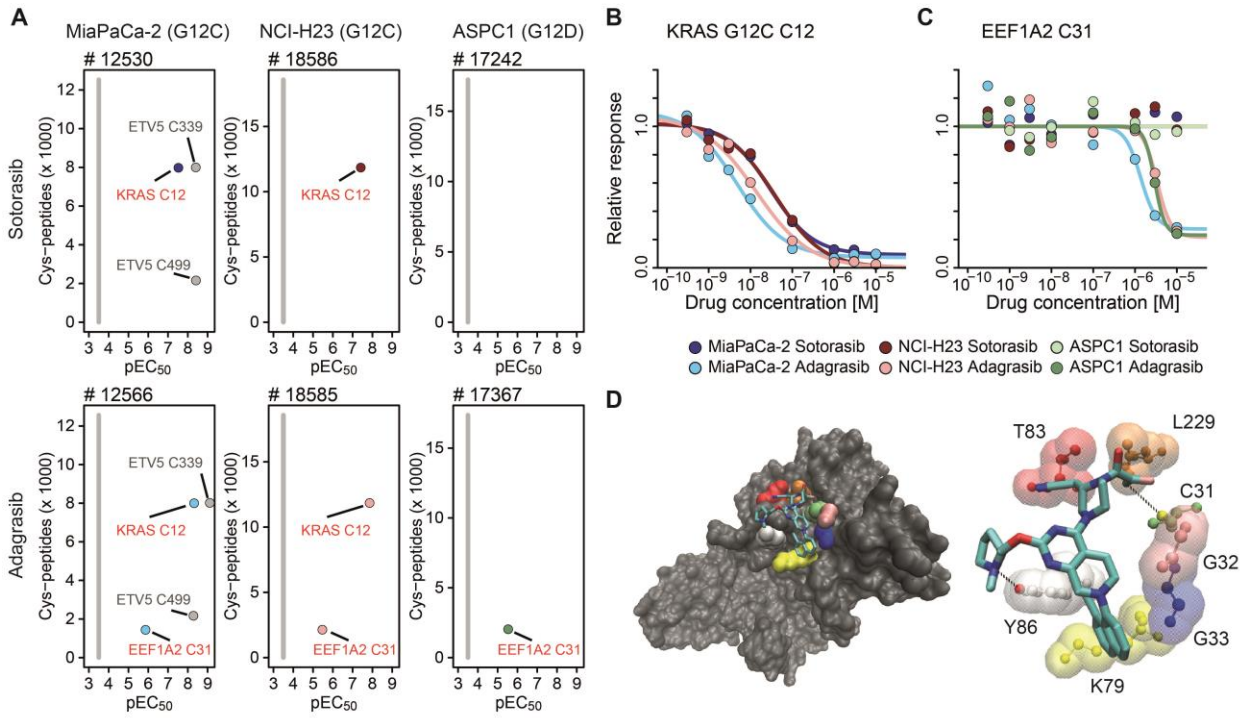

Fig. 2. DecryptC profiling of clinical KRAS G12C inhibitors in KRAS mutant lines. (A) Number of concentration-response curves (y-axis) and potency [$pEC_{50} = -\log10(EC_{50})$, x-axis] of cys-peptides following 2 h treatment of MiaPaCa-2, NCI-H23, or ASPC1 cells with sotorasib or adagrasib ($n \geq 8$). Targets of sotorasib and/or adagrasib are highlighted in color, all other cys-peptides are displayed in grey. **(B and C)** Concentration-response curves for the primary sotorasib and adagrasib target KRAS G12C Cys^{12} (B) and for the adagrasib off-target EEF1A2 Cys^{31} (B) (2 h, $n \geq 8$). **(D)** The left panel shows molecular docking of adagrasib into the structure of EEF1A2 (PDB ID: 8B6Z). The right panel depicts molecular interactions of adagrasib with amino acid residues of EEF1A2 bringing the reactive enolate group into close proximity to Cys^{31} to enable its covalent modification. For all panels, data represent *n* sets of

cells per experiment, each treated with a different drug concentration; recalibrated and fold-change-adjusted F-statistics by CurveCurator.

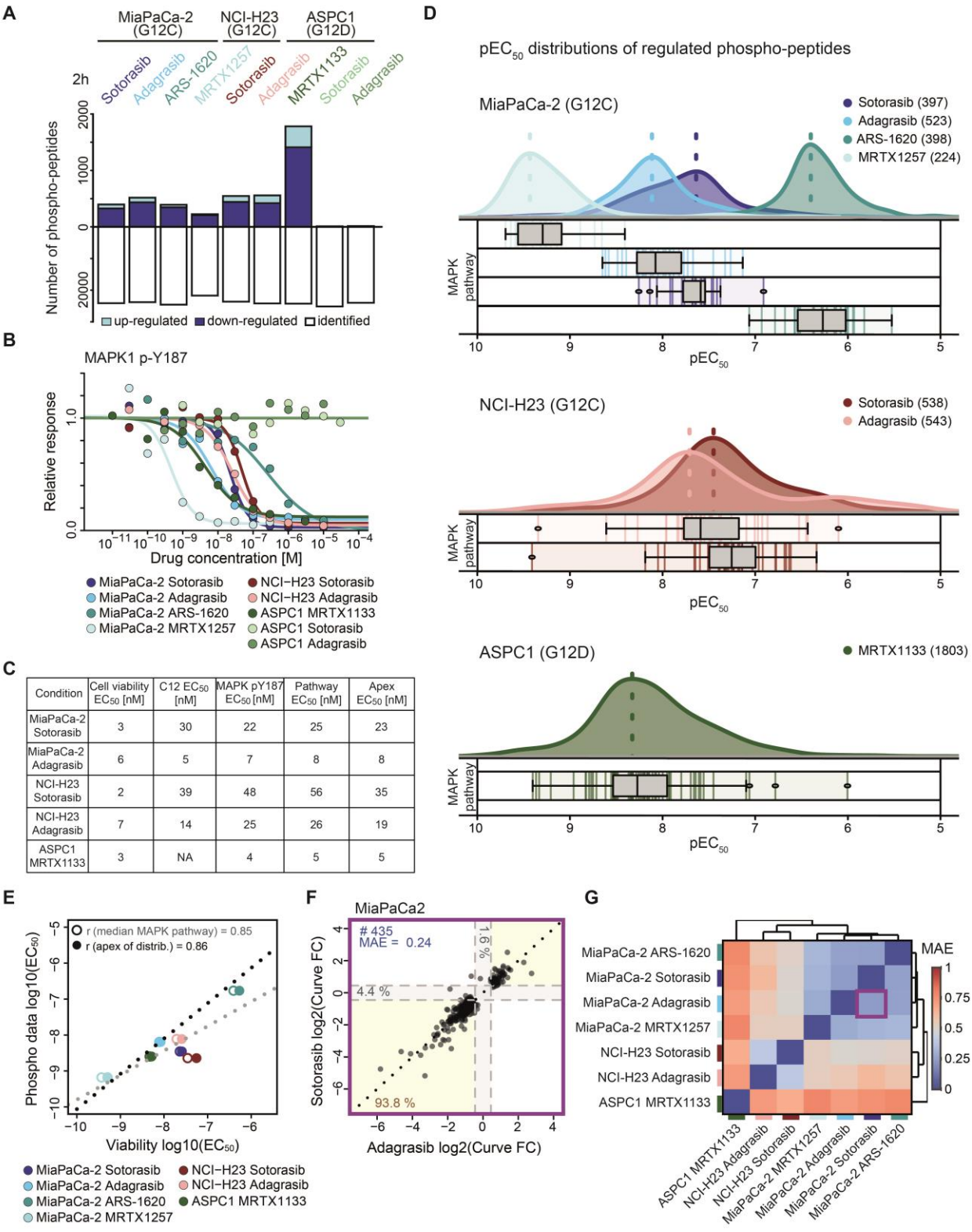

Condition	Cell viability EC_{50} [nM]	C12 EC_{50} [nM]	MAPK pY187 EC_{50} [nM]	Pathway EC_{50} [nM]	Apex EC_{50} [nM]
MiaPaCa-2 Sotorasib	3	30	22	25	23
MiaPaCa-2 Adagrasib	6	5	7	8	8
NCI-H23 Sotorasib	2	39	48	56	35
NCI-H23 Adagrasib	7	14	25	26	19
ASPC1 MRTX1133	3	NA	4	5	5

Fig. 3. DecryptM profiling of KRAS inhibitors in mutant KRAS cell lines. (A) Number of identified and drug-regulated phosphopeptides in three mutant KRAS cell lines after short-term (2 h) drug treatment (n ≥ 10). **(B)** Concentration-response curves for MAPK1 (Tyr^{187}) activation

loop phosphorylation in the same cell lines and using the same drugs as in panel (A) (2 h; n ≥ 10). **(C)** Summary of the potency of drug response at the level of cell viability (72 h, n ≥ 9), KRAS Cys^{12} target binding (2 h, n ≥ 8), MAPK1 (Tyr^{187}) activation loop phosphorylation (2 h; n ≥ 10), drug-regulated phosphopeptides from KEGG-annotated MAPK pathway members (2 h, hsa04010; median $pEC_{50} = -\log10(EC_{50})$) and all drug-regulated phosphopeptides (apex pEC_{50}, 2 h, n ≥ 10). **(D)** The distribution of drug potency ($pEC_{50} = -\log10(EC_{50})$) determined for all phosphopeptides with abundance changes in each cell line treated with the indicated drug (2 h; n ≥ 10). Numbers following drug names indicate the number of regulated phosphopeptides detected in the experiment. Dashed line indicates the maximum of the distribution (apex). The boxplots show pEC_{50} values for phosphopeptides on proteins annotated as MAPK pathway members (KEGG: hsa04010). The box indicates the median and interquartile range (IQR); whiskers indicate 1.5× IQR values. **(E)** Correlation analysis of $\log10(EC_{50})$ values determined for drug-induced cell viability (72 h, n ≥ 9) and phosphopeptide abundance changes (2 h, n ≥ 10) either using phosphopeptides with concentration-dependent abundance changes originating from annotated MAPK pathway members only or the apex of the pEC_{50} distribution from all drug-regulated phosphopeptides for each individual treatment (r: Pearson correlation coefficient). **(F)** Scatter plot comparing the log2 curve fold changes of phosphopeptides with concentration-dependent abundance changes to adagrasib and/or sotorasib in MiaPaCa-2 cells. Dashed lines mark the fold change boundary of the applied CurveCurator log2 fold change cut-off (fc-value = ±0.45; n ≥ 10). Dotted lines represents the diagonal (x=y). Yellow areas contain phosphopeptides with consistent responses, grey areas contain phosphopeptides regulated by one of the conditions only. Percentages indicate the fraction of phosphopeptides in the regions highlighted by color. MAE: mean absolute error of log2 curve fold changes. **(G)** Cluster map summarizing the data exemplified in panel (F) (purple box) for all KRAS drugs and cell lines based on hierarchical clustering of the mean absolute error (MAE) of log2 curve fold changes (2 h; n ≥ 10). For all data panels, *n* represent sets of cells per experiment, each treated with a different drug concentration; recalibrated and fold-change-adjusted F-statistics by CurveCurator.

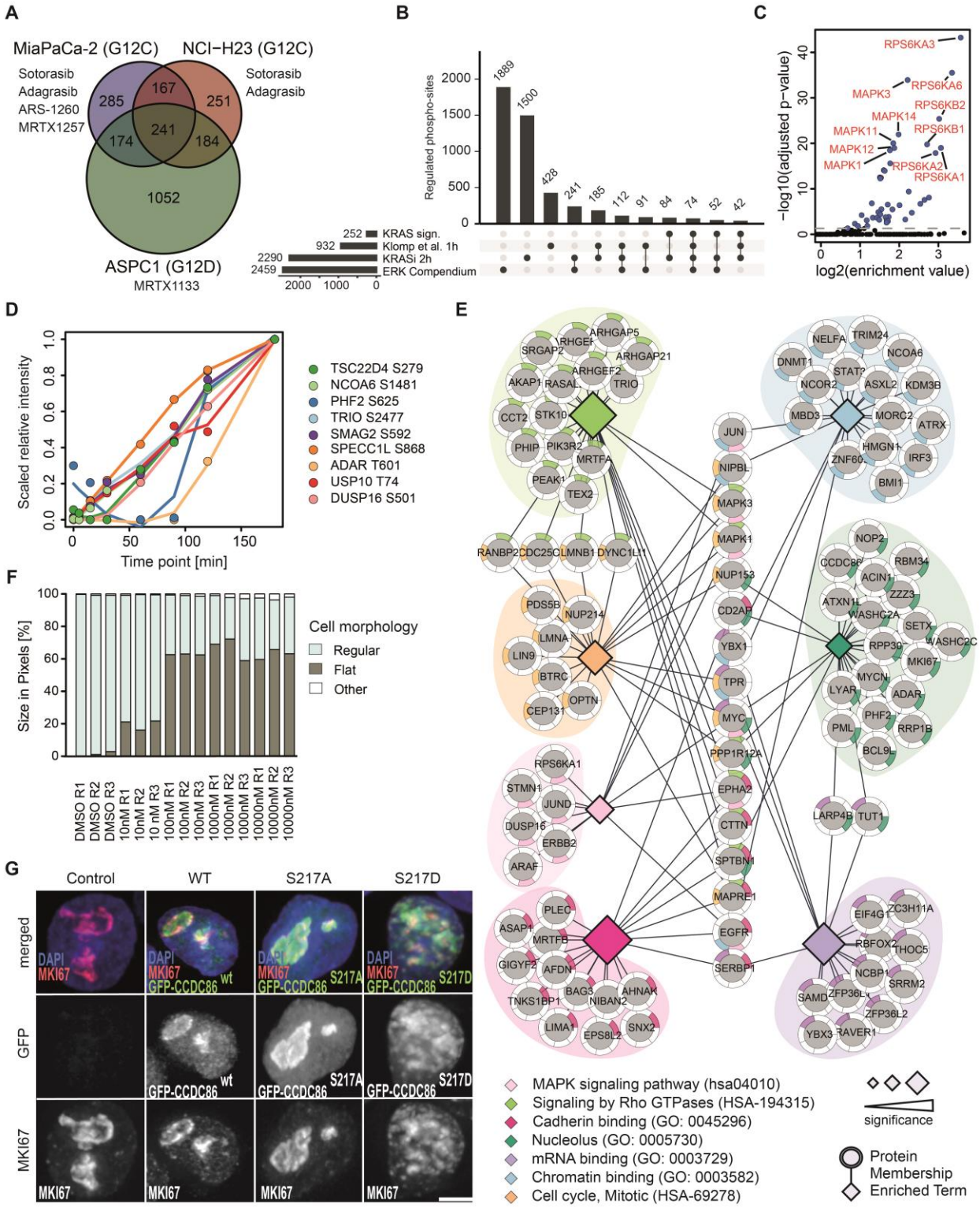
A
MiaPaCa-2 (G12C)
NCI−H23 (G12C)
Sotorasib
Adagrasib
ARS-1260
MRTX1257
Sotorasib
Adagrasib
285
167
251
241
174
184
1052
ASPC1 (G12D)
MRTX1133
B
Regulated phospho-sites
1889
1500
428
241
185
112
91
84
74
52
42
252 KRAS sign.
932 Klomp et al. 1h
2290 KRASi 2h
2459 ERK Compendium
C
−log10(adjusted p−value)
log2(enrichment value)
RPS6KA3
MAPK3
RPS6KA6
RPS6KB2
MAPK14
MAPK11
RPS6KB1
MAPK12
MAPK1
RPS6KA2
RPS6KA1
D
Scaled relative intensity
Time point [min]
TSC22D4 S279
NCOA6 S1481
PHF2 S625
TRIO S2477
SMAG2 S592
SPECC1L S868
ADAR T601
USP10 T74
DUSP16 S501
E
F
Size in Pixels [%]
Cell morphology
Regular
Flat
Other
DMSO R1
DMSO R2
DMSO R3
10nM R1
10nM R2
10 nM R3
100nM R1
100nM R2
100nM R3
1000nM R1
1000nM R2
1000nM R3
10000nM R1
10000nM R2
10000nM R3
G
Control
WT
S217A
S217D
merged
GFP
MKI67
DAPI
MKI67
GFP-CCDC86 wt
GFP-CCDC86 S217A
GFP-CCDC86 S217D
MAPK signaling pathway (hsa04010)
Signaling by Rho GTPases (HSA-194315)
Cadherin binding (GO: 0045296)
Nucleolus (GO: 0005730)
mRNA binding (GO: 0003729)
Chromatin binding (GO: 0003582)
Cell cycle, Mitotic (HSA-69278)
significance
Protein
Membership
Enriched Term

Fig. 4. Cellular processes impacted by a KRAS core signaling signature. (A) Venn diagram of drug-regulated phosphopeptides detected in MiaPaCa-2 (KRAS G12C), NCI-H23 (KRAS G12C), and ASPC1 (KRAS G12D) cells defining a common KRAS core signaling signature of 241 phosphopeptides (2 h; n ≥ 10 sets of cells per experiment, each treated with a different drug concentration; recalibrated and fold-change-adjusted F-statistics by CurveCurator). **(B)** Upset plot comparing data from this study (252 phosphosites on the 241 phosphopeptides that comprise the KRAS core signaling signature and all 2,290 phosphosites on the 2,354 phosphopeptides regulated by all KRAS drugs after 2 h of treatment) to two published molecular resources of ERK signaling (the ERK-regulated phosphoproteome, denoted as Klomp *et al*. and the ERK compendium (*8, 11*)). **(C)** Kinase motif enrichment analysis of decreased phosphopeptides from the KRAS core signaling signature. **(D)** Time-resolved increase of synthetic peptide phosphorylation from MAPK1 in vitro kinase assays representing putative MAPK1 substrates from the list of 241 phosphopeptides comprising the KRAS core signaling signature (n = 8 technical replicates). For clarity, the response of the assay was scaled from 0 to 1. **(E)** Graphical representation of enriched biological processes of proteins underlying the KRAS core signaling signature. The size of the diamond node for each enriched gene set was scaled by the statistical significance of the functional enrichment analysis (based on functional enrichment analysis, adjusted p-val. ≤ 0.05). Protein nodes with more than one color in the halo map to more than one enrichment term. **(F)** Quantification of cell morphology features of MiaPaCa-2 cells in response to sotorasib (72 h, n = 3 sets of cells per concentration). **(G)** Representative images of NCI-H23 cells untransfected (control) or transfected with either GFP–CCDC86 WT, GFP–CCDC86 S217A, or GFP–CCDC86 S217D constructs (green) 24h post-transfection. Cells were also stained for MKI67 (red) and DNA (DAPI). Scale bar, 5 µm.

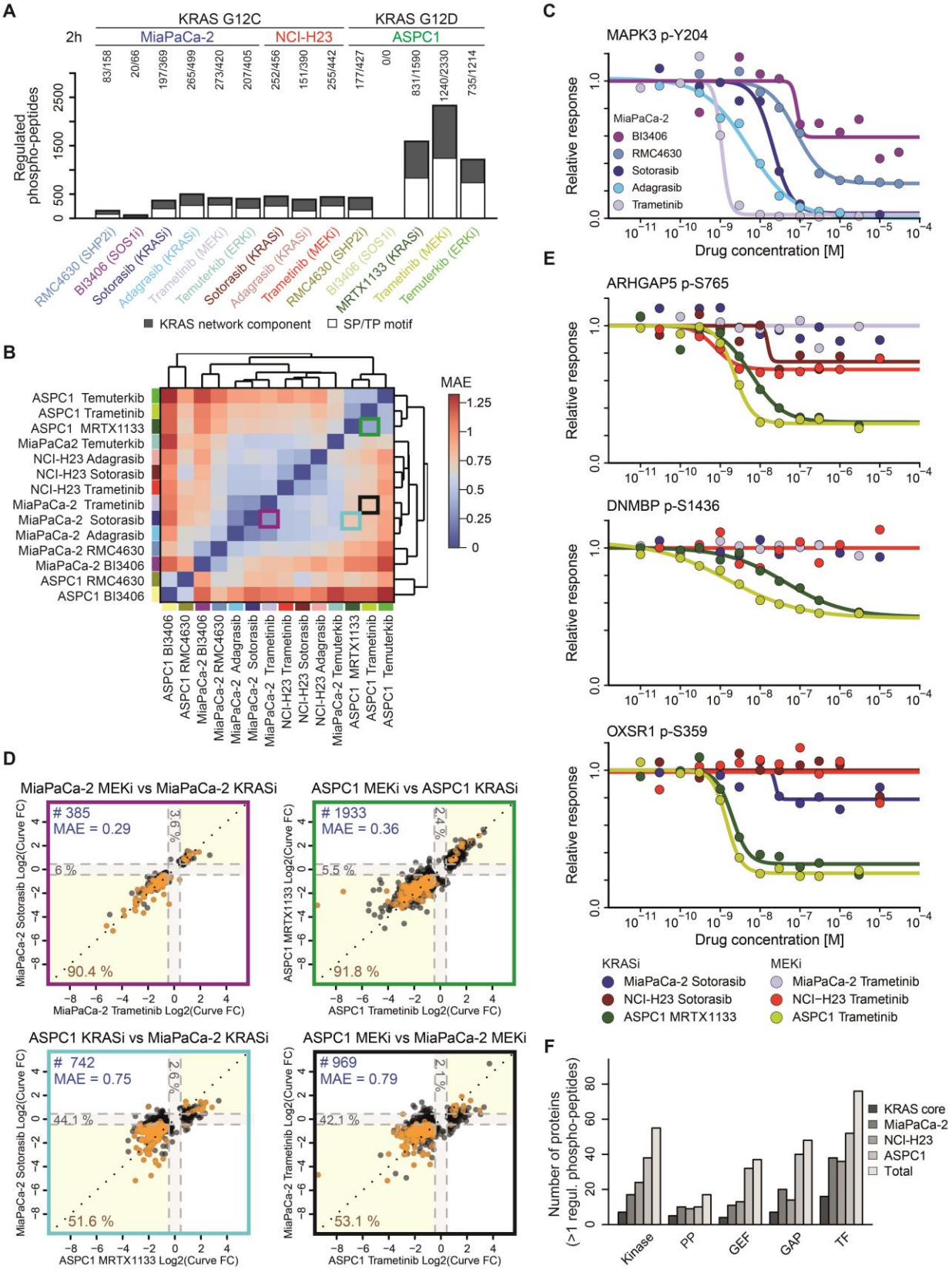

Fig. 5. Cell line-specific KRAS signaling. (A) Number of phosphopeptides showing concentration-dependent abundance changes in response to BI3406 (SOS1i), RMC4630 (SHP2i),

sotorasib (KRASi; G12C), adagrasib (KRASi; G12C), MRTX1133 (KRASi; G12D), trametinib (MEKi) and temuterkib (ERKi) after 2 h of drug exposure in three mutant KRAS cell lines ($n \geq 10$). The white part of each bar represents the number of phosphopeptides containing an SP or TP phosphorylation motif. Numbers on the top of each bar specify the number of phosphopeptides in the white and black parts of a bar. **(B)** Cluster map based on hierarchical clustering of the mean absolute error (MAE) summarizing the pairwise comparisons of phosphopeptide responses across all combinations of SOS1i, SHP2i, KRASi, MEKi and ERKi inhibitors and cell lines from panel (A). MAE, mean absolute error of log2 curve fold changes ($n \geq 10$). **(C)** Concentration-response curves of MAPK3 Tyr^{204} phosphorylation (activation loop) in response to 5 MAPK pathway modulating drugs (MiaPaCa-2; $n \geq 10$). **(D)** Pairwise comparisons of responses (log2 curve fold change) of phosphopeptides with concentration-dependent abundance changes for different combinations of drugs and cell lines shown in (B) ($n \geq 10$). Dashed lines mark the fold change boundary of the applied CurveCurator log2 fold change cut-off (fc-value = ±0.45). Dotted lines represents the diagonal (x=y). Percentages indicate the fraction of phosphopeptides in the regions highlighted by color. Yellow areas contain phosphopeptides with consistent responses, grey areas contain phosphopeptides regulated by one of the conditions only. Orange data points mark phosphopeptides from the KRAS core signaling signature. MAE: mean absolute error of log2 curve fold changes. **(E)** Example phosphopeptides showing concentration-dependent responsiveness in one cell line (ASPC1) but no or weak responses in other cell lines ($n \geq 10$). **(F)** Number of kinases, phosphatases (PP), guanine nucleotide exchange factors (GEFs), GTPase-activating proteins (GAPs), and transcription factors (TF) that showed drug-induced regulation of at least one phosphopeptide in the different cell lines upon KRAS inhibition. For all panels, data represent *n* sets of cells per experiment, each treated with a different drug concentration; recalibrated and fold-change-adjusted F-statistics by CurveCurator.

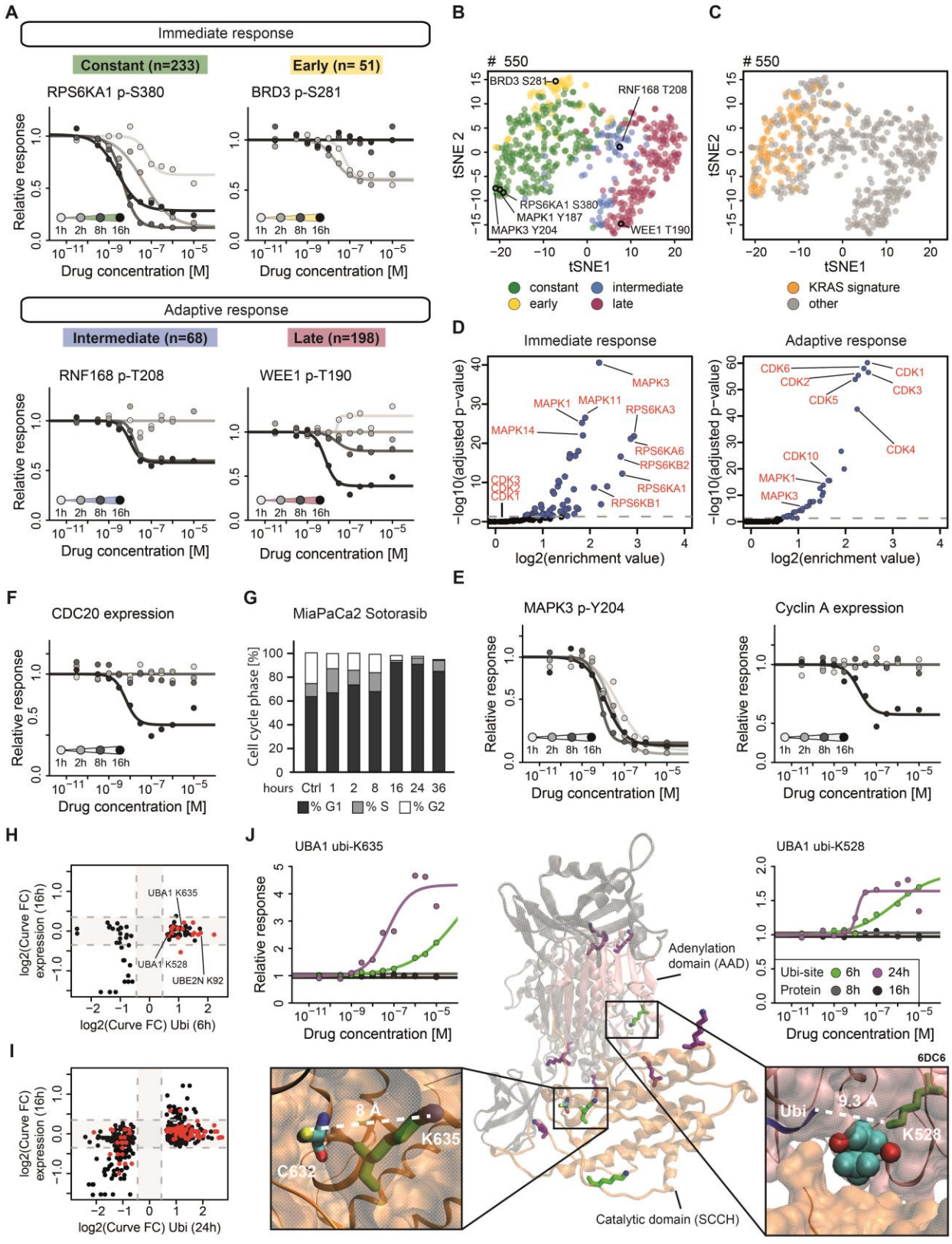
A
Immediate response
Constant (n=233)
Early (n= 51)
RPS6KA1 p-S380
BRD3 p-S281
Relative response
Drug concentration [M]
1h 2h 8h 16h
Adaptive response
Intermediate (n=68)
Late (n=198)
RNF168 p-T208
WEE1 p-T190
B
550
BRD3 S281
RNF168 T208
RPS6KA1 S380
MAPK1 Y187
MAPK3 Y204
WEE1 T190
tSNE 2
tSNE1
constant
intermediate
early
late
C
550
tSNE2
tSNE1
KRAS signature
other
D
Immediate response
Adaptive response
−log10(adjusted p−value)
log2(enrichment value)
MAPK3
MAPK1
MAPK11
RPS6KA3
MAPK14
RPS6KA6
RPS6KB2
RPS6KA1
RPS6KB1
CDK3
CDK2
CDK1
CDK6
CDK2
CDK1
CDK3
CDK5
CDK4
CDK10
MAPK1
MAPK3
E
MAPK3 p-Y204
Cyclin A expression
F
CDC20 expression
G
MiaPaCa2 Sotorasib
Cell cycle phase [%]
hours Ctrl 1 2 8 16 24 36
% G1
% S
% G2
H
UBA1 K635
UBA1 K528
UBE2N K92
log2(Curve FC) expression (16h)
log2(Curve FC) Ubi (6h)
I
log2(Curve FC) Ubi (24h)
J
UBA1 ubi-K635
UBA1 ubi-K528
Adenylation domain (AAD)
Ubi-site 6h 24h
Protein 8h 16h
6DC6
8 Å
K635
C632
9.3 Å
Ubi
K528
Catalytic domain (SCCH)

Fig. 6. Temporal response of the proteome, phosphoproteome and ubiquitinome of MiaPaCa-2 cells to sotorasib. (A) Example concentration-response curves for phosphopeptides that showed constant (green), early (yellow), intermediate (blue), or late (red) response to 1-16 h of sotorasib treatment (n = 11). **(B)** t-SNE plot of responses (abs. log2 curve fold change) of phosphopeptides detected at all four time points (1, 2, 8, and 16 h) and regulated in at least one condition colored by the groups defined in (A) (n = 11). # denotes the number of phosphopeptides in the plot. **(C)** Same as (B) but highlighting members of the KRAS core signaling signature. **(D)** Kinase motif enrichment analysis of decreased phosphopeptides from the constant/early groups (immediate response; left panel) or intermediate/late groups (adaptive response; right panel). **(E)** Concentration-response curves of MAPK Tyr^{204} phosphorylation and Cyclin A (CCNA2) protein abundance at the four time points (n = 11). **(F)** Concentration-response curves of protein abundance of the cell cycle–regulating protein CDC20 (n = 11). **(G)** Barplot summarizing FACS-based cell cycle analysis data (propidium iodide staining) following different durations of sotorasib treatment in MiaPaCa-2 cells (300 nM; 0-36 h, control = Ctrl; n = 7 independent experiments). **(H and I)** Scatter plot comparing protein abundance changes (16 h) against peptide ubiquitylation at 6 h (H) and 24 h (I) (n = 11). Shown are only significantly regulated ubiqutinylated peptides. Proteins of the ubiquitin conjugation system are highlighted in red (Uniprot KW_0833). Dashed lines mark the fold change boundary of the applied CurveCurator log2 fold change cut-off (ubiquitin data: fc-value = ±0.45; protein abundance data: fc-values = ±0.35). Grey areas contain ubiquitylated peptides without corresponding changes in protein abundance**(J)** Alphafold structure of UBA1 (*83*) highlights the adenylation domain (pink) and catalytic SCCH domain (orange) as well as drug-regulated ubiquitylated lysine residues after 6 h (green) or 24 h (purple) of sotorasib treatment. Magnified views of the structure show the catalytic domain highlighting drug-regulated ubiquitylated Lys^{635} (green) in close proximity to the catalytic Cys^{632} residue based on Alphafold structure of UBA1 and the co-crystal structure of UBA1 (PDB: 6DC6) (*84*), ATP(β,γ)+Mg (cyan an d red), and ubiquitin (blue) highlighting the close proximity of the active site to Lys^{528} (green). Graphs show the concentration-response curves of UBA1 Lys^{635} and Lys^{528} ubiquitylation after 6 h (light green) and 24 h (purple) of sotorasib treatment as well as protein abundance changes of UBA1 after 6 h (dark grey) and 16 h (black) (n = 11). For all panels presenting proteomics data, data represent *n* sets of cells per experiment, each treated with a different drug concentration; recalibrated and fold-change-adjusted F-statistics by CurveCurator.